Targeted autophagy disruption reveals the central role of macrophage iron metabolism in systemic iron homeostasis

Meriem Taleb, Isabelle Maillet, Marc Le Bert, Catherine Mura

Targeted autophagy disruption reveals the central role of macrophage iron metabolism in systemic iron homeostasis

Meriem Taleb [1,2] Isabelle Maillet[1], Marc Le Bert[1], and Catherine Mura[*,1,2]

[1]Experimental and Molecular Immunology and Neurogenetics, UMR 7355 CNRS, Orléans, France; [2]University of Orléans, Orléans, France

Short title: Macrophages and systemic iron homeostasis

Key points

● Autophagy deficiency in macrophages results in systemic parenchymal iron overload

● Erythropoietic macrophages with autophagy deficiency accumulate the iron exporter ferrorportin and have low hepcidin expression.

Corresponding author:
Catherine Mura
UMR7355, 3B rue de la Ferollerie
45071 Orléans, France
email : catherine.mura@cnrs-orleans.fr
phone: +33 238 25 79 75
fax: +33 238 25 79 79

Abstract word counts : 243

Text word counts : 3992

Figure/table count : 7 figures, 1 table

Reference count : 80

ABSTRACT

Iron homeostasis depends on both intracellular control through iron-responsive proteins and the systemic level of iron through hepcidin-ferroportin axis. Indeed, the hormone hepcidin downregulates the ferroportin iron exporter to control iron recycling from macrophages and iron uptake from enterocytes. Here, we focused on the role of autophagy in macrophage iron metabolism and systemic iron homeostasis. Mice deficient for autophagy in macrophages (*LysM-Atg5*$^{-/-}$) mimicked a primary iron overload phenotype, resulting in high ferroportin expression in both macrophages and enterocytes that correlated with marked parenchymal iron overload. Furthermore, *LysM-Atg5*$^{-/-}$ mice exhibited increased hematopoietic activity with no sign of anemia but correlating with rather high plasma iron level. Compared to wild-type cells, bone marrow-derived macrophages from *LysM-Atg5*$^{-/-}$ mice had significantly increased ferroportin expression and a decreased iron content, confirming high iron export. In erythrophagocytic macrophages, autophagy regulates hemosiderin storage mechanisms as well as the degradation of ferroportin and subsequently its plasma membrane localization and iron export; furthermore, ferroportin colocalization with hepcidin indicates hepcidin autocrine activity. Relatively high hepatic hepcidin expression, and decreased hepcidin level in the spleen of *LysM-Atg5*$^{-/-}$ mice correlating with low hemosiderin iron storage as well as in erythrophagocytic *Atg5*$^{-/-}$ macrophages were evidenced. Therefore, our results highlight the critical role of autophagy in macrophages for iron trafficking and systemic iron homeostasis. We propose that in macrophages, autophagy restricts ferroportin level and iron export resulting in hepcidin expression with an autocrine-paracrine effect that takes part in the regulation of the ferroportin expression in duodenal enterocytes.

KEY WORDS

Autophagy • Macrophages • Ferroportin • Iron homeostasis.

Visual abstract

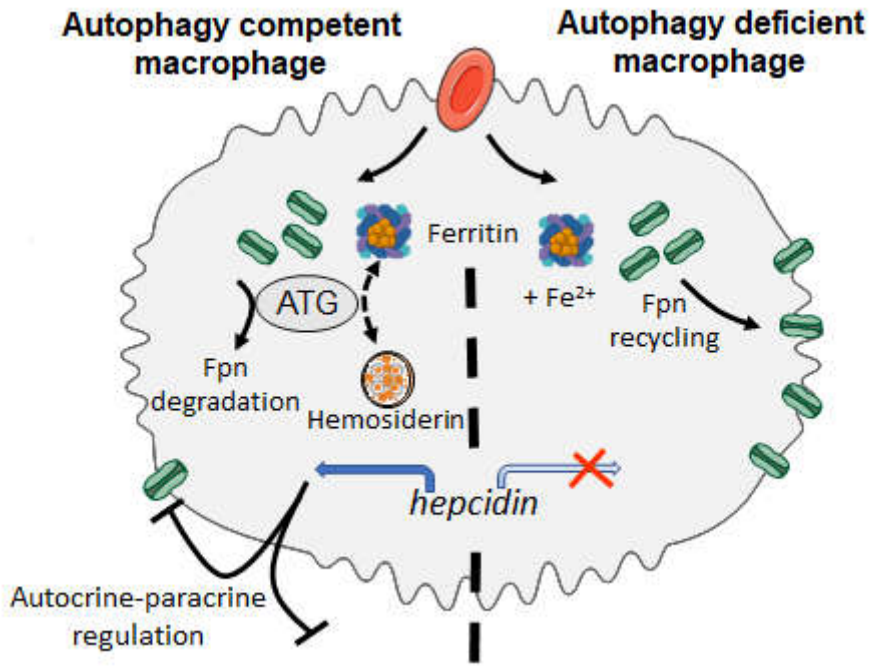

INTRODUCTION

In mammals, iron metabolism is achieved through a complex network of specialized proteins responsible for iron uptake, transport and storage. Most body iron (~75%) is mobilized in the form of heme in erythrocytes.[1] Macrophages recycle iron after phagocytosis of senescent or damaged red blood cells (RBCs) and act as nursing cells to support erythropoiesis;[2] when iron is present in excess hepatocytes preferentially accumulate iron.[1-4] In addition, dietary iron uptake through duodenal enterocytes plays an essential role building the postnatal iron stock and satisfying iron demand. The ferroportin (FPN) iron exporter is mainly found in macrophages and duodenal enterocytes and releases ferrous iron into the blood.[5,6] There, after oxidation via ceruloplasmin and hephaestin, transferrin traffics ferric iron, which is subsequently acquired by cells through transferrin receptor 1 (TfR1)-mediated endocytosis.[7-9]

It is generally accepted that the hepatic peptide hormone hepcidin (HAMP) is the key regulator of systemic iron trafficking through negative control of ferroportin by inducing its degradation.[9-11] Hepcidin, which is also expressed at low levels in macrophages and in other cells (eg heart, brain, kidney), may exert local tissue-specific functions. Hepcidin transcription is upregulated in response to elevated transferrin saturation, iron stores, and inflammation and is suppressed by hypoxia and erythropoiesis.[12-16] Ferroportin is also transcriptionally regulated independently of hepcidin in response to iron, erythrophagocytosis, hypoxia and inflammation.[17-22]

After TfR1-mediated endocytosis, iron is released from transferrin by STEAP3 metalloreductase and DMT1 metal transporter.[23-26] In cells, only small amounts of reactive ferrous labile iron are readily available for immediate use or export. Indeed, iron is stored in a nontoxic and bioavailable ferric form in H/L ferritin heteropolymer shells.[27] Alternatively, high cellular iron levels, mainly erythrophagocytic macrophages and hepatocytes, promote the accumulation of hemosiderin, a lysosomal degradation complex localized within endomembrane structures (siderosomes).[3] The release of iron from ferritin primarily relies on ferritinophagy, a selective autophagic process, involving the specifc cargo molecule nuclear receptor coactivator 4 (NCOA4) delivering ferritin to lysosomes.[28,29] In the cytosol, ferrous ions are trafficked by binding to iron chaperones of the nuclear ribonucleoprotein family, the poly r(C) binding proteins (PCBPs).[30-34] The intracellular iron balance is maintained by the coordinated posttranscriptional regulation of a series of key proteins through cytoplasmic

sensors of labile iron, namely iron regulatory proteins IRP1 and IRP2, which notably inversely regulate TfR1—*i.e.,* iron absorption— and ferritin— *i.e.,* iron storage.[35]

Defects in the hepcidin gene itself or in genes encoding positive regulators of hepcidin (hemojuvelin, HFE, TfR2, and BMPs),[9,10,36] or ferroportin mutant unresponsive to hepcidin,[37] lead to unrestricted expression of membrane ferroportin, resulting in low iron levels in macrophages and enterocytes, increased serum iron indices and systemic parenchymal iron overload. A series of gene defects that include DMT1$^{-/-}$, STEAP3$^{-/-}$, NCO4$^{-/-}$, IRP2$^{-/-}$, and the mutations causing aceruloplasminemia, hypo-transferrinemia and dominant ferroportin disease are characterized by decreased iron mobilization that compromises hematopoiesis but leads to tissue iron overload via compensatory enterocyte iron uptake.[29,38-47] The increased liver hepcidin level consistent with elevated iron stores observed in these mouse models fails to limit ferroportin-mediated iron export from macrophages and enterocytes, suggesting the involvement of an additional mechanism independent of liver hepcidin signaling.

We hypothesized that macrophage iron trafficking may play a role in systemic iron homeostasis and questioned autophagy disruption. Autophagy is a mammalian system for delivering intracellular components to lysosomes for degradation or recycling. Under starvation conditions, autophagy is induced to generate nutrients and energy through degradation of macromolecules and organelles, but under nutrient-rich conditions, constitutive autophagy has a protective quality control function to degrade protein aggregates, organelles and pathogens.[48,49] Deletion of one of the genes encoding a core autophagy-related protein (ATG) results in ineffective autophagy and causes either embryonic or neonatal lethality due to defects in nutrient supply, recycling or waste disposal.[50] Autophagy-related 5 gene (*Atg5*) expression in the brain rescues the lethal phenotype of *Atg5* deficiency in mice, but, despite normal organ histology, results in iron acquisition and growth impairments with anemia, and unproper regulation of iron-related gene expression.[51] Here, mice with targeted *Atg5* deletion in monocyte/granulocyte progenitors (*LysM-Atg5*$^{-/-}$) had dysregulated iron trafficking, ferroportin mislocalization and low hepcidin expression in macrophages.They also had a systemic iron overload phenotype and elevated liver hepcidin levels. Indeed, autophagy in macrophage plays a critical role in intracellular ferroportin turnover, affects iron distribution through insufficient hepcidin expression and autocrine-paracrine activity.

MATERIALS AND METHODS

Animals

LysM-Atg5$^{-/-}$ mice on C57BL/6J background were generated by crossing the *Atg5* floxed (*Atg5*$^{fl/fl}$) mice[52] with *lysozyme M cre* (*LysM cre*) transgenic strain.[53] Details about animal breeding, care and management are provided in the supplemental Methods. Genotyping primers and antibody for Atg5 immunodetection are listed in supplemental Table 1.

Hematology, serum and iron parameters

Hematological parameters, serum and iron parameters, nonheme tissue iron content were analyzed as described previously[54,55] and detailed in the supplemental Methods.

Histology, immunofluorescence, dot blot, protein analysis and quantitative PCR

Conventional procedures as described in the supplemental Methods were used; primer sequences and antibodies are listed in supplemental Table 1 and 2.

Flow cytometric analysis

Single-cell suspensions of femoral bone marrow (BM) cells and blood cells were obtained as described previously[54] and detailed in the supplemental Methods. Cell immunostaining and flow cytometric analysis were carried out in accordance with standard procedures (supplemental Methods), and erythroid precursors staining was as previously described.[56] For the FACS-calcein assay, cells collected in PBS were incubated for 15 min with 0.2 µM calcein acetoxymethyl ester (calcein-AM, Sigma Chemicals) probe, fluorescence was detected in the FITC channel.

Bone marrow-derived macrophages and treatments

Bone marrow-derived macrophage (BMDM) preparation and treatments are described in the supplemental Methods. Opsonized red blood cells were prepared as described in Kovtunovych *et al*.[57]

Statistical analysis

GraphPad Prism software was used for statistical analyses and detailed in the supplemental Methods.

RESULTS

Autophagy deficiency in myeloid cells results in high erythropoietic activity and mild liver fibrosis

We sought to determine the role of autophagy in iron metabolism—and more specifically, in macrophages—by using conditional knockout mice deficient for *Atg5* in myeloid macrophage/granulocyte lineage cells *(LysM-Atg5$^{-/-}$)*. The genotype of floxed mice was confirmed by PCR (supplemental Figure 1A). The birth of *LysM-Atg5$^{-/-}$* mice at the expected Mendelian ratio indicated that Atg5 in macrophages was not essential for mouse embryonic development. Immunofluorescence analysis revealed specific Atg5 deletion in macrophages of spleen and liver, as well as in bone marrow-derived macrophages, from *LysM-Atg5$^{-/-}$* mice (supplemental Figure 1B). Although *LysM-Atg5$^{-/-}$* mice maintained on a standard diet developed normally to adulthood without overt abnormalities (until 18 months) and were fertile, they had a reduced body weight compared with age- and sex-matched littermate wild-type (WT) controls (-5.59 g ±1.58 for both male and female mice, supplemental Figure 1C). *LysM-Atg5$^{-/-}$* mice had normal counts of peripheral myeloid blood cells, including monocyte, granulocyte neutrophil and eosinophil subsets (supplemental Figure 1D).

The livers of *LysM-Atg5$^{-/-}$* mice weighed less at 6-8 months and showed a noticeably lighter color than WT controls (Figure 1A-B), with normal liver histology and similar distribution of Kupffer cells (Figure 1B). Furthermore, low-grade liver fibrosis (Figure 1B), and, in some cases, the presence of widely distributed lipid droplets, characteristic of mild steatosis was revealed in the hepatic parenchyma of *LysM-Atg5$^{-/-}$* compared to WT mice (supplemental Figure 2A). No overt signs of liver injury were detected in terms of the serum transaminases AST (Figure 1C) and ALT (not shown), inflammatory markers and cell infiltration (Figure 1A H&E, supplemental Figure 2B).

The spleens of *LysM-Atg5$^{-/-}$* mice were darker and larger than those of WT (Figure 2A), however with similar distribution of macrophage subpopulations of the red pulp (F4/80^{+}) and marginal zone (F4/80^{-} CD11b^{+}) (Figure 2B, supplemental Figure 3A). The red pulp reservoir of erythrophagocytic macrophages in *LysM-Atg5$^{-/-}$* mice appeared lighter and contained significantly less visible hemosiderin pigment than that in WT controls (Figure 2Ci). Moreover, increased numbers of erythroblastic islands, where erythroid precursors develop, and red blood cells, as evidenced by the increased cellularity in the subcapsular red pulp, were clearly identified in the spleen of *LysM-Atg5$^{-/-}$* mice. Flow cytometric analysis confirmed

extramedullary erythropoietic activity with increased splenic $CD71^+$ $Ter\text{-}119^+$ immature erythroid precursors in *LysM-Atg5*$^{-/-}$ mice (Figure 2Ci, supplemental Figure 3B).

The bone marrow of *LysM-Atg5*$^{-/-}$ mice revealed higher erythropoietic activity with an increased cell density and early erythroid precursor population compared with WT controls (Figure 2Cii, supplemental Figure 3B). The peripheral red blood cell indices, blood smears and flow cytometric analysis results documented the absence of red blood cell abnormalities in terms of number, shape and size in *LysM-Atg5*$^{-/-}$ mice, and similar levels of circulating bilirubin, erythropoietin (Figure 2Ciii, supplemental Figure 3B, Table 1) and bone marrow erythroferrone mRNA (not shown), to WT mice. A mild increase in immature red blood cells was observed in *LysM-Atg5*$^{-/-}$ mice compared to WT controls, which usually results from premature cell release from tissues accompanying high erythropoietic activity. A higher level of serum iron and a moderately higher transferrin saturation (TS) were observed in *LysM-Atg5*$^{-/-}$ than in WT mice, whereas the total iron binding capacity (TIBC) and serum ferritin (SF) level were similar in both mice (Table 1). Thus, Atg5 deficiency in myeloid cells tended to increase iron release into blood and its utilization for erythropoiesis without signs of anemia.

Increased ferroportin plasma membrane expression in macrophages and enterocytes of *LysM-Atg5*$^{-/-}$ mice with systemic iron overload

A large amount of Perl's stainable-nonheme iron naturally present in macrophages primarily as hemosiderin, was observed in the spleens of WT mice, whereas *LysM-Atg5*$^{-/-}$ mice had a severely reduced amount of nonheme ferric iron in macrophages of the splenic red pulp (Figure 3A). However, the total splenic iron content rather similar in both mice (Figure 3Bi) indicates higher heme iron in *LysM-Atg5*$^{-/-}$ mice, correlated with increased erythropoiesis. Further, the splenic ferric ferritin content was significantly higher in *LysM-Atg5*$^{-/-}$ mice than WT mice, although ferritin expression was similar thus indicating lower iron in the form of hemosiderin in *LysM-Atg5*$^{-/-}$ mice. The calcein fluorescence quenching assay indicated higher cytosolic labile iron pool in splenic macrophages ($F4/80^+CD11b^-$) and monocytes ($F4/80^-CD11b^+$) (Figure 3C), as well as bone marrow myeloid $CD11b^+Ly6C/G^+$ (supplemental Figure 4Ai) cell subsets, from *LysM-Atg5*$^{-/-}$ than WT mice. Immunofluorescence revealed a marked increase of ferroportin in splenic macrophages from *LysM-Atg5*$^{-/-}$ mice, with accumulation at the plasma membrane in isolated splenic macrophages (Figure 3D) and nucleated bone marrow cells (supplemental Figure 4Aii) of *LysM-Atg5*$^{-/-}$ mice. In contrast, splenic macrophages of WT mice showed a predominantly ponctuated intracellular localization of ferroportin and little plasma

membrane staining (Figure 3D). Therefore, these results indicated high iron mobilization from macrophages in *LysM-Atg5*$^{-/-}$ mice, consistent with the increased erythropoiesis.

Since the duodenum and liver are critical for iron homeostasis, we analyzed these tissues in *LysM-Atg5*$^{-/-}$ mice. The duodenum of *LysM-Atg5*$^{-/-}$ mice was longer than that of WT mice (37 cm versus 35 cm for male mice, p-value = 0.0012). Unexpectedly, *LysM-Atg5*$^{-/-}$ mice showed marked duodenal iron absorption evidenced by a drastic deficiency of nonheme iron deposition in enterocytes of the superior part of the duodenum (Figure 3A). Furthermore, in parts of the duodenum where food was still in transit, nonheme iron was stained in the apical and basal compartments of enterocytes from *LysM-Atg5*$^{-/-}$mice suggesting iron flux to export, while enterocytes from WT mice showed iron mostly blocked within the apical compartment (Figure 3A). The iron depletion in the duodena in *LysM-Atg5*$^{-/-}$ mice correlated with low duodenal level of ferric iron-loaded ferritin and ferritin H (Ft-H) expression (Figure 3Bii). High ferroportin protein expression and accumulation along the basolateral plasma membrane of enterocytes and along the intestinal villi of the proximal duodenum were revealed in *LysM-Atg5*$^{-/-}$ mice, whereas barely detectable in WT mice (Figure 3Bii, 3D).

In the livers of WT mice, nonheme iron staining was observed in Kupffer cells, *i.e.,* resident hepatic sinusoidal macrophages, and in the hepatocytes limited to the portal area of the liver lobules (Figure 3A). In contrast, *LysM-Atg5*$^{-/-}$ mice had markedly increased nonheme stainable iron deposition in hepatocytes, with a gradient extending from the portal area to the centrilobular area along the blood flow, but sparse staining in Kupffer cells (Figure 3A, supplemental Figure 4B). The hepatic nonheme iron level correlated with the elevated total tissue iron content and the ferric ferritin iron content and ferritin H expression levels (Figure 3Biii). In both *LysM-Atg5*$^{-/-}$ and WT livers, ferroportin was scarcely detected in hepatocytes (supplemental Figure 4B). A full investigation of the iron distribution in *LysM-Atg5*$^{-/-}$ mice showed a systemic parenchymal iron accumulation within acinar cells of the exocrine pancreas, convoluted tubules in the renal medulla, cardiac muscle cells and testicular arteriolar cells, with significantly increased iron content in the kidney and pancreas (supplemental Figure 4C). Thus, Atg5-mediated autophagy deficiency in macrophages results in redistribution of iron stores with increased ferric ferritin, plasma membrane ferroportin expression in enterocytes and macrophages, and elevated iron deposition in parenchymal tissues, indicating high iron uptake, in *LysM-Atg5*$^{-/-}$ mice compared to WT mice.

Dysregulation of iron homeostasis in *LysM-Atg5*$^{-/-}$ mice consistent with low hepcidin expression in macrophages

Accumulation of ferroportin at the cell surface membrane of macrophages and the basolateral membrane of enterocytes in *LysM-Atg5*$^{-/-}$ mice might depend on the expression of hepcidin. Indeed, we showed that the hepatic mRNA level of *Hamp1*, encoding hepcidin, was increased in *LysM-Atg5*$^{-/-}$ mice (Figure 4Ai). The expression levels of *Id1* and *Fga*, two well-established markers of activation of Smad and Stat, which control the major signaling pathways positively regulating hepcidin expression, showed that *Id1* mRNA expression was increased in the livers of *LysM-Atg5*$^{-/-}$ mice compared to WT mice and correlated with *Hamp1* expression, while *Fga* expression was unaffected (Figure 4Ai). However, the ratio of hepcidin mRNA level to hepatic iron content was low (Figure 4Aii). Further, the immunodetected hepcidin was increased around the portal veins in the liver of *LysM-Atg5*$^{-/-}$ mice (Figure 4Aiii). The levels of serum hepcidin in *LysM-Atg5*$^{-/-}$ mice was higher than in WT mice (Figure 4B).

In the spleen of *LysM-Atg5*$^{-/-}$ mice, higher ferroportin levels and lower levels of iron than those in WT mice, correlated with a significantly lower level of *Hamp1* mRNA expression (Figure 4Ci). Further, compared to WT, in *LysM-Atg5*$^{-/-}$ mice a lower level of hepcidin protein was localized on splenic macrophages and preferentially within the outmost region farthest from blood vessels (Figure 4Ci-ii) where an iron load was also observed in macrophages. In the duodenum, hepcidin spread on the basal membrane of the enterocytes and macrophages of the duodenal mucosa of wild-type mice, whereas scarcely detected in *LysM-Atg5*$^{-/-}$ mice (Figure 4D). Therefore, despite the increase in hepatic expression of hepcidin with hepatic iron overload, the elevated level of plasma membrane ferroportin in macrophages and enterocytes in *LysM-Atg5*$^{-/-}$ mice indicated insufficient production of hepcidin in this pathologic condition to restrict membrane ferroportin from macrophages and enterocytes.

Atg5 deficiency in macrophages resulted in mislocalization of ferroportin and high iron efflux

We next focused on the role of autophagy in macrophage iron uptake, distribution and sensing. After differentiation, bone marrow-derived macrophages (BMDMs) were treated with ferric ammonium citrate (FAC), holo-transferrin (holo-TF), or opsonized red blood cells (oRBCs). We verified that *Atg5*$^{-/-}$ and wild-type BMDMs incubated under all conditions had similar viability, membrane integrity, and cellular activity and mitochondrial dehydrogenase activity (supplemental Figure 5A).

Under all conditions, in addition to the lack of Atg5 expression, *Atg5*$^{-/-}$ BMDMs accumulated p62/SQSTM1 a widely used autophagy marker whose degradation in autolysosomes is dependent on the autophagy activity (Figure 5Ai). Compared with WT BMDMs, untreated

Atg5$^{-/-}$ BMDMs had higher membrane ferroportin levels (Figure 5Ai), higher basal calcein fluorescence, *i.e.,* a decrease in the cellular labile iron pool and higher membrane TfR1 levels (Figure 5B, supplemental Figure 5B), that indicate higher iron export.

Incubation with FAC (16h) led to marked calcein quenching, *i.e*., an increase in the labile iron pool, in both *Atg5*$^{-/-}$ and WT BMDMs, whereas the intracellular labile iron pool was barely affected in either cell type after incubation with holo-TF or oRBCs compared to control incubation (Figure 5B). Both WT and *Atg5*$^{-/-}$ BMDMs incubated with FAC and oRBCs exhibited high ferric ferritin (Fe-Ft-H) accumulation (Figure 5Aii), concomitant with increased ferritin H and HO-1 expression (Figure 5Ai), as well as ROS levels after oRBCs treatment (Figure 5B); incubation with holo-TF resulted in a modest increase in ferric ferritin levels. Therefore, autophagy deficiency did not impair iron uptake or ferritin iron storage.

The kinetics of BMDMs treated with oRBCs revealed a strong expression of Hif2α and *Hmox1* at 2-4h, indicating heme catabolism concomitant with nonheme iron accumulation, in both WT and *Atg5*$^{-/-}$ BMDMs (Figures 6A-B-Ci, supplemental Figure 6Ai). In WT erythrophagocytic BMDMs, after an apparent decrease of p62/SQSTM1 and LC3I (which was likely due to an increase of proteins from RBCs), a decrease in p62/SQSTM1 protein level at 16 to 24 hours and increased conversion of cytosolic LC3I into the lipidated II form were observed, indicating autophagy activation (Figure 6A). In both WT and *Atg5*$^{-/-}$ macrophages, at early time points (30 min-1h) densitometric analysis revealed an increase in ferroportin from membrane proteins extracts whereas ferroportin gene expression markedly increased at later time points (8-16h), correlating with the high intracellular iron content (Figure 6A-B-Ci, supplemental Figure 6Ai), and indicating that high amount of ferroportin derived from red blood cells. After 8-16h, ferroportin drastically decreased from membrane protein extracts (Figure 6A) and was localized in perinuclear aggregates, which looked like aggresomes (Figure 6Cii, supplemental Figure 6Aii). In WT macrophages, ferroportin colocalized with Atg5 in cytoplasmic vesicles as soon as 8h peaking at 16h (Figure 6D, supplemental Figure 6B). Further, in *Atg5*$^{-/-}$ BMDMs higher levels of ferroportin relocated to the membranes at 24h compared to WT cells (Figures 6A-6Cii, supplemental Figure 6Aii), indicating impaired degradation of ferroportin through autophagy in *Atg5*$^{-/-}$ macrophages.

Hepcidin mRNA expression increased at 2-8h in WT cells (Figure 6B) but less in *Atg5*$^{-/-}$ (Figure 6B). Intracellular hepcidin colocalized with ferroportin in the periphery of aggresomes, peaking at 12h, at a lower level in *Atg5*$^{-/-}$ than in WT cells, indicating that hepcidin is involved in autocrine signaling for ferroportin proteasomal degradation (Figure 6E, supplemental Figure

6C). Overall, both proteasomal and autophagy degrade the ferroportin in erythrophagocytic macrophages. Further, the *Fpn* mRNA expression at 16h may contribute to the membrane protein turnover. However, in *Atg5*$^{-/-}$ macrophages the lack of functional autophagy and low hepcidin expression impaired ferroportin degradation after erythrophagocytosis that led to increased plasma membrane ferroportin expression.

DISCUSSION

Here, we focused on the role of autophagy in macrophage iron metabolism. We show that in macrophages, after erythrophagocytosis, the ferroportin from the rich membrane of red blood cells[59] accumulates in perinuclear aggregates, or aggresome, the holding stations of proteins for autophagy process. While in wild-type macrophages the ferroportin is largely degraded, autophagy-deficiency in *Atg5*$^{-/-}$ macrophages compromises intracellular ferroportin degradation resulting in a high level of ferroportin protein relocalization on the plasma membrane. Cells use two main routes for degrading intracellular proteins, the ubiquitin-proteasome and autophagy-lysosome pathways, which are coordinated.[60] Notably, protein accumulation in a single juxtanuclear aggresome has been observed in pathological and non-pathological situations.[61] The disassembly and clearance of aggresomes depend both on proteasomal activity[62] and efficient capture into autophagic structures.[63-65] It has been previously shown that turnover of DMT1, the transporter for iron uptake into enterocytes and iron egress from endosomes during the transferrin cycle, as well as TfR1 are controlled through both proteasomal and lysosomal-autophagic degradation, and deficiency of degradation impairs iron homeostasis.[66-68] Here, our results reveal that in macrophages, erythrophagocytosis activates autophagy then used as the main process for ferroportin protein degradation and turnover, and thus to control the level of iron release, whereas proteasomal protein degradation may be sufficient in cells with low ferroportin turnover.

LysM-Atg5$^{-/-}$ mice had drastically reduced levels of splenic Perl's stainable ferric iron but a relatively high ferric ferritin content. In cells, nonheme iron is stored in ferritin complexes in a manner primarily related to the iron concentration. However, over a high iron concentration range, iron-loaded ferritin complexes are converted into hemosiderin complexes, membrane vesicles produced after lysosomal degradation that predominate in macrophages.[3,69-71] Therefore, in macrophages of *LysM-Atg5*$^{-/-}$ mice autophagy deficiency impairs the shift from fully loaded ferritin to the hemosiderin compartment, this leading to an increase in iron mobilization from its storage site[72] and thus participates in its cell release.

In wild-type BMDMs, hepcidin expression increases early after erythrophagocytosis and colocalisation with ferroportin indicate that hepcidin would be involved as autocrine signal for ferroportin degradation. In *LysM-Atg5*$^{-/-}$ mice, high liver hepcidin correlated whith high iron content and low ferroportin in hepatocytes, whereas ferroportin was high in macrophages and enterocytes. Comparison of WT and hepcidin KO mice[73] revealed that liver hepcidin produced in WT degrades the hepatocyte ferroportin but is not sufficient to degrade the macrophage

ferroportin, indicating the primarily autocrine role of hepcidin. At the systemic level, conditional deletion of the essential autophagy gene *Atg5* in macrophages led to the accumulation of the ferroportin at the plasma membrane in macrophages and, unexpectedly, at the basolateral membrane in absorptive enterocytes where it plays a major role in iron export to blood. These observations are consistent with the relatively low level of iron in splenic macrophages. The rather high blood iron indices and increased erythropoietic activity in the bone marrow and spleen without signs of anemic stress corroborated the uncontrolled iron efflux and iron mobilization for erythropoiesis in *LysM-Atg5*$^{-/-}$ mice. Furthermore, high iron efflux correlated with systemic parenchymal iron overload, primarily in hepatocytes, and increased hepatic expression of hepcidin. However, the increased hepatic level of hepcidin, as well as serum level, in *LysM-Atg5*$^{-/-}$ mice failed to limit ferroportin-mediated iron export from macrophages and enterocytes. Mice deficient for autophagy in macrophages are characterized by cellular iron depletion and low hepcidin expression, while rather high levels of hepcidin and ferroportin proteins localized to macrophages indicate insufficient hepcidin to degrade the elevated level of membrane ferroportin. It has been shown that elevated liver iron levels modulate hepcidin expression even in mice overexpressing Epo, thus limiting the maximum hepcidin expression level.[74] In *LysM-Atg5*$^{-/-}$ mice, the absence of erythropoietic demand indicates that another signal may be implicated in systemic ferroportin control. We observed that *LysM-Atg5*$^{-/-}$ mouse spleens have lower levels of hepcidin than WT mouse spleens, conversely to hepatic and serum hepcidin levels, indicating thus that macrophages would contribute to systemic iron regulation (Figure 7).

Human disorders and knockout mouse models related to iron-modulating proteins have provided important insights into the maintenance of iron homeostasis. Dominant ferroportin disease results in iron accumulation in macrophages, mild anemia with low transferrin saturation but hyperferritinemia, and increased liver iron and hepcidin levels.[47,75] In this disease, it has been shown that ferroportin accumulates in intracellular vesicles from erythrophagocytic macrophages and thus has less efficient relocalization to membrane. Furthermore, inhibition of endocytosis leads to complete redistribution of ferroportin on the plasma membrane in WT macrophages.[75] Therefore, ferroportin likely traffics between the plasma membrane and endomembrane in WT macrophages, and it has been suggested that ferroportin can localize in hemosiderin structures.[76-78]

Furthermore, both iron treatment and erythrophagocytosis increase ferroportin transcription and induce ferroportin relocalization to the plasma membrane in WT macrophages.[18,78]

Macrophages represent an essential compartment for iron homeostasis, and the process of autophagy affects ferroportin trafficking and turnover. The deficiency of autophagy in macrophages impairs proper ferroportin degradation and turnover after erythrophagocytosis and increases its relocalization to the plasma membrane that leads excess iron release from macrophages and enterocytes that triggers increased erythropoiesis and parenchymal iron overload.

A large amount of iron traffics to macrophages and accumulating data suggest that tissue macrophages are ferrostats that sense and respond to local tissue iron needs, thereby regulating iron availability in the local microenvironment and contributing to systemic iron homeostasis.[79] Here in *LysM-Atg5*$^{-/-}$ mice, increased membrane ferroportin level in enterocytes and splenic macrophages was consistent with low expression of hepcidin by macrophages and insufficient expression by hepatocytes. Taken together, our results in mice with autophagy-deficient macrophages provide new insight into the major role of the macrophages in iron sensing and systemic iron homeostasis. In macrophages, the lack of ferroportin degradation led to a low labile iron content and decreased hepcidin expression. Thus, we propose that the unrestricted membrane ferroportin expression observed in enterocytes result from autocrine-paracrine regulation of ferroportin by hepcidin expression in widely distributed resident macrophages.

ACKNOWLEDGMENTS

The authors thank Valérie Quesniaux and Bernhard Ryffel (Unité Mixte de Recherche 7355, Centre National de la Recherche Scientifique [CNRS], Oléans, France) for helpful discussion. The authors acknowledge David Gosset of the P@CYFIC platform for fluorescent Zeiss microscopy imaging (Center for Molecular Biophysics, Unité Propre de Recherche 4301, CNRS, Orléans, 45071 France).

This study was supported by CNRS and University Orléans, 'Fondation pour la Recherche Médicale (grant EQU202003010405) and European funding in Region Centre-Val de Loire (European Regional Development Fund grant EX005756 and EX010381). M.T. received thesis financial support from Region Centre-Val de Loire. M.T. is a PhD candidate at University of Orléans, and this work is submitted in partial fulfillment of the requirement for her thesis).

AUTHORSHIP

Contribution : M.T. performed most experiments, analyzed data, made the figures and contributed to write the manuscript; I.M. performed experiments ; M.L.B. carried out breeding and gene testing to produce the conditional *LysMAtg5-/-* mice ; C.M. designed the research, analyzed data and wrote the paper.

Conflict-of-interest disclosure : The authors declare no competing financial interests.

ORCID profile : M.L.B., 0000-0002-5945-3800. ; C.M., 0000-0002-8414-1139.

Correspondence: Catherine Mura, UMR7355, 3B rue de la Ferollerie , 45071 Orléans, France; e-mail : catherine.mura@cnrs-orleans.fr.

REFERENCES

1- Korolnek T, Hamza I. Macrophages and iron trafficking at the birth and death of red cells. *Blood*. 2015;125(19):2893-2897.

2- May A, Forrester LM. The erythroblastic island niche: modeling in health, stress, and disease. *Exp Hematol*. 2020;91:10-21.

3- Iancu TC. Ferritin and hemosiderin in pathological tissues. *Electron Microsc Rev*. 1992;5:209-229.

4- Nairz M, Theurl I, Swirski FK, Weiss G. ‘‘Pumping iron’’ how macrophages handle iron at the systemic, microenvironmental, and cellular levels. *Pflugers Arch.* 2017;469(3):397-418.

5- Donovan A, Lima CA, Pinkus JL, Zon LI, Robine S, Andrews NC. The iron exporter ferroportin/Slc40a1 is essential for iron homeostasis. *Cell Metab*. 2005;1(3):191-200.

6- McKie AT, Marciani P, Rolfs A, *et al*. A novel duodenal iron-regulated transporter, IREG1, implicated in the basolateral transfer of iron to the circulation. *Mol Cell*. 2000;5:299-309.

7- Yoshida K, Furihata K, Takeda S. *et al*. A mutation in the ceruloplasmin genes is associated with systemic hemosiderosis in humans. *Nat Genet.* 1995;9(3):267-272.

8- Vulpe CD, Kuo YM, Murphy TL, *et al*. Hephaestin, a ceruloplasmin homologue implicated in intestinal iron transport, is defective in the sla mouse. *Nat Genet*. 1999;21(2):195–199.

9- Muckenthaler MU, Rivella S, Hentze MW, Galy B. A red carpet for iron metabolism. *Cell.* 2017;168(3):344-361.

10- Nicolas G, Bennoun M, Devaux I, *et al*. Lack of hepcidin gene expression and severe tissue iron overload in upstream stimulatory factor 2 (*USF2*) knockout mice. *Proc Natl Acad Sc USA* 2001;98(15):8780-8785.

11- Nemeth E, Tuttle MS, Powelson J, *et al*. Hepcidin regulates cellular iron efflux by binding to ferroportin and inducing its internalization. *Science.* 2004;306 (5704):2090-2093.

12- Pigeon C, Ilyin G, Courselaud B, *et al*. A new mouse liver-specific gene, encoding a protein homologous to human antimicrobial peptide hepcidin, is overexpressed during iron overload. *J Biol Chem.* 2001;276(11):7811-7819.

13- Nicolas G, Chauvet C, Viatte L, *et al*. The gene encoding the iron regulatory peptide hepcidin is regulated by anemia, hypoxia, and inflammation. *J Clin Invest.* 2002;110(7):1037-1044.

14- Nemeth E, Valore EV, Territo M, Schiller G, Lichtenstein A, Ganz T. Hepcidin, a putative mediator of anemia of inflammation, is a type II acute-phase protein. *Blood.* 2003;101(7):2461-2463.

15- Liu Q, Davidoff O, Niss K, Haase VH. Hypoxia-inducible factor regulates hepcidin via erythropoietin-induced erythropoiesis. *J Clin Invest*. 2012;122(12):4635-4644.

16- Kautz L, Jung G, Valore EV, Rivella S, Nemeth E, Ganz T. Identification of erythroferrone as an erythroid regulator of iron metabolism. *Nat Genet.* 2014;46(7):678–684.

17- Delaby C, Pilard N, Gonçalves AS, Beaumont C, Canonne-Hergaux F. Presence of the iron exporter ferroportin at the plasma membrane of macrophages is enhanced by iron loading and down-regulated by hepcidin. *Blood.* 2005;106(106):3979-3984.

18- Knutson MK, Vafa MR, Haile DJ, Wessling-Resnick M. Iron loading and erythrophagocytosis increase ferroportin 1 (FPN1) expression in J774 macrophages. *Blood.* 2003;102(12):4191-4197.

19- Yang F, Liu XB, Quinones M, Melby PC, Ghio A, Haile DJ. Regulation of reticulendothelial iron transporter MTP1 (Slc11a3) by inflammation. *J. Biol. Chem*. 2002;277(42):39786-39791.

20- Mastrogiannaki M, Matak P, Delga S, Deschemin JC, Vaulont S, Peyssonnaux C. Deletion of HIF-2α in the enterocytes decreases the severity of tissue iron loading in hepcidin knockout mice. *Blood.* 2012;119(2):587-590.

21- Taylor M, Qu A, Anderson ER, *et al*. Hypoxia-inducible factor-2α mediates the adaptive increase of intestinal ferroportin during iron deficiency in mice. *Gastroenterology.* 2011;140(7):2044-2055.

22- Marro S, Chiabrando D, Messana E., *et al*. Heme controls ferroportin1 (FPN1) transcription involving Bach1, Nrf2 and MARE/ARE sesquence motif at position -7007 of the FPN1 promoter. *Hematologica.* 2010;95(8):1261-1268.

23- Levy JE, Jin O, Fujiwara Y, Kuo F, Andrews NC. Transferrin receptor is necessary for development of erythrocytes and the nervous system. *Nat Genet.* 1999;21(4):396-399.

24- Ohgami RS, Campagna DR, Antiochos B, *et al*. *nm1054*: a spontaneous, recessive, hypochromic, microcytic anemia mutation in the mouse. *Blood*. 2005;106(10):3625-3631.

25- Gunshin H, Mackenzie B, Berger UV, *et al*. Cloning and characterization of a mammalian proton-coupled metal-ion transporter. *Nature.* 1997;388(6641):482-488.

26- Tabuchi M, Yanatori I, Kawai Y, Kishi F. Retromer-mediated direct sorting is required for proper endosomal recycling of the mammalian iron transporter DMT1. *J Cell Science*. 2009;123(5):756-766.

27- Ferreira C, Bucchini D, Martin ME, *et al*. Early embryonic letality of H ferritin gene deletion in mice. *J Biol Chem.* 2000;275(5):3021-3024.

28- Dowdle WE, Nyfeler B, Nagel J, *et al*. Selective VPS34 inhibitor blocks autophagy and uncovers a role for NCOA4 in ferritin degradation and iron homeostasis *in vivo. Nat Cell Biol.* 2014 ;16:1069-1079.

29- Bellelli R, Federico G, Matte A, *et al*. NCOA4 deficiency impairs systemic iron homeostasis. *Cell Reports* 2016;14(3):411–421.

30- Shi H, Bencze KZ, Stemmler TL, Philpott CC. A cytosolic iron chaperone that delivers iron to ferritin. *Science*. 2008;320(5580):1207–1210.

31- Yanatori I, Yasui Y, Tabuchi M, Kishi F. Chaperone protein involved in transmembrane transport of iron. *Biochem J.* 2014;462(1):25-37.

32- Lane DJR, Richardson DR. Chaperone turns gatekeeper : PCBP2 and DMT1 form an iron-transport pipeline. *Biochem J*. 2014;462(1):e1-e3.

33- Yanatori I, Richardson DR, Imada K, Kishi F. Iron export through the transporter ferroportin 1 is modulated by the chaperone PCBP2. *J Biol Chem.* 2016;291(33):17303-18.

34- Yanatori I, Richardson DR, Toyokuni S, Kishi F. How iron is handled in the course of heme catabolism: Integration of heme oxygenase with intracellular iron transport mechanisms mediated by poly (rC)-binding protein-2. *Arch Biochem Biophys*. 2019;672:108071.

35- Muckenthaler MU, Galy B, Hentze M. Systemic Iron Homeostasis and the Iron-Responsive Element/Iron-Regulatory Protein (IRE/IRP) Regulatory Network. *Annu Rev Nutr.* 2008;28:197-213.

36- Ganz T, Nemeth E. Regulation of iron acquisition and iron distribution in mammals. *Biochim Biophys Acta.* 2006;1763(7):690–699.

37-Altamura S, Kessler R, Gröne HJ, *et al*. Resistance of ferroportin to hepcidin binding causes exocrine pancreatic failure and fatal iron overload. *Cell Metab*. 2014;20(2):359-367.

38- Gunshin H, Fujiwara Y, Custodio AO, DiRenzo C, Robine S, Andrews NC. Slc11a2 is required for intestinal iron absorption and erythropoiesis but dispensable in placenta and liver. *J Clin Invest.* 2005;115(5):1258-1266.

39- Ohgami RS, Campagna DR, Greer EL, *et al*. Identification of a ferrireductase required for efficient transferrin-dependent iron uptake in erythroid cells. *Nat Genetics.* 2005;37:1264-1269.

40- Galy B, Ferring D, Minana B, *et al*. Altered body iron distribution and microcytosis in mice deficient in iron regulatory protein 2 (IRP2). *Blood.* 2005;106(7):2580-2589.

41- LaVaute T, Smith S, Cooperman S, *et al*. Targeted deletion of the gene encoding iron regulatory protein-2 causes misregulation of iron metabolism and neurodegenerative disease in mice. *Nat Genet.* 2001;27(2):209–214.

42- Harris Z L, Durley AP, Man, TK, Gitlin JD. Targeted gene disruption reveals an essential role for ceruloplasmin in cellular iron efflux. *Pro Natl Acd Sc. USA* 1999;96(19):10812-10817.

43- Kenawi M, Rouger E, Island ML, *et al.* Ceruloplasmin deficiency does not induce macrophagic iron overload: lessons from a new rat model of hereditary aceruloplasminemia. *FASEB J. 2019;*33(12):13492–13502.

44- Hayashi A, Wada Y, Suzuki T, Shimizu A. Studies on familial hypotransferrinemia: unique clinical course and molecular pathology. *Am J Hum Genet.* 1993;53(1):201-213.

45- Athiyarath R, Arora N, Fuster F, *et al*. Two novel missense mutations in iron transport protein transferrin causing hypochromic microcytic anaemia and haemosiderosis: molecular characterization and structural implications. *Br J Haematol.* 2013;163(3):404–420.

46- Fuqua BK, Lu Y, Fraze DM, *et al*. Severe iron metabolism defects in mice with double knockout of the multicopper ferroxidases hephaestin and ceruloplasmin. *Cell Mol Gastroenterol Hepatol.* 2018;6(4):405-427.

47- Pietrangelo A. The ferroportin disease. *Blood Cells Mol Dis*. 2004;32(1):31–138.

48- Boya P, Reggiori F, Codogno P. Emerging regulation and functions of autophagy. *Nature Cell Biol*. 2013 ;15(7):713-720.

49- Galluzzi L, Green DR. Autophagy-independent functions of the autophagy machinery. *Cell*. 2019;177(7):1682-1699.

50- Kuma A, Hatano M, Matsui M, et al. The role of autophagy during the early neonatal starvation period. *Nature.* 2004;432(7020):1032–1036.

51-Yoshii SR, Kuma A, Akashi T, et al. Systemic analysis of Atg5-null mice rescued from neonatal lethality by transgenic ATG5 expression in neurons. *Dev Cell.* 2016;39(1):116–130.

52- Hara T, Nakamura K, Matsui M, *et al*. Suppression of basal autophagy in neural cells causes neurodegenerative disease in mice. *Nature*. 2006 ;441(7095):885-889.

53- Clausen BE, Burkhardt C, Reith W, Renkawitz R, Förster I. Conditional gene targeting in macrophages and granulocytes using LysMcre mice. *Transgenic Res*.1999; 8(4) :265-277.

54- Agoro R, Benmerzoug S, Rose S, *et al*. An iron-rich diet decreases the mycobacterial burden and correlates with hepcidin upregulation, lower levels of proinflammatory mediators, and increased T-cell recruitment in a model of *Mycobacterium bovis* Bacille Calmette-Guerin infection. *J Infect Dis*. 2017;216(7):907–918.

55- Agoro R, Taleb M, Quesniaux VFJ, Mura C. Cell iron status influences macrophage polarization. *Plos One*. 2018;13(5):e0196921.

56- Koulnis M, Pop R, Porpiglia Er, Shearstone JR, Hidalgo D, Socolovsky M. Identification and analysis of mouse erythroid progenitors using the CD71/TER119 Flow-cytometric Assay. *J Vis Exp.* 2011;54:e2809.

57- Kovtunovych G, Eckhaus MA, Ghosh MC, Ollivierre-Wilson H, Rouault TA. Dysfunction of the heme recycling system in heme oxygenase 1–deficient mice: effects on macrophage viability and tissue iron distribution. *Blood.* 2010;116(26):6054-6062.

58- Raha-Chowdhury R, Raha AA, Forostyak S, Zhao JW, Stott SRW, Bomford A. Expression and cellular localization of hepcidin mRNA and protein in normal rat brain. *BMC Neurosci*. 2015 ;16:24.

59- Zhang DL, Senecal T, Ghosh MC, Ollivierre-Wilson H, Tu T, Rouault TA. Hepcidin regulates ferroportin expression and intracellular iron homeostasis of erythroblasts. *Blood*. 2011 ; 118(10):2868-2877.

60- Liebl MP and Hoppe T. It's all about talking: two-way communication between proteasomal and lysosomal degradation pathways via ubiquitin. *Am J Physiol Cell Physiol.* 2016;311(2):C166–C178.

61- Kopito RR. Aggresomes, inclusion bodies and protein aggregation. *Trends Cell Biol*. 2000;10:524-530.

62- Hao R, Nanduri P, Rao Y, *et al*. Proteasomes activate aggresome disassembly and clearance by producing unanchored ubiquitin chains. *Mol Cell.* 2013;51:819-828.

63- Garcia-Mata R, Gao YS, Sztul E. Hassles with taking out the garbage: aggravating aggresomes. *Traffic.* 2002;3:388-396.

64- Fortun J, Dunn Jr WA, Joy S, Li J, Notterpek L. Emerging role for autophagy in the removal of aggresomes in schwann cells. *J Neurosci*. 2003;23(33):10672-10680.

65- Wong ESP, Tan JMM, Soong WE, *et al*. Autophagy-mediated clearance of aggresomes is not a universal phenomenon. *Hum Mol Genet*. 2008;17(16):2570–2582.

66- Garrick MD, Zhao L, Roth JA, *et al*. Isoform specific regulation of divalent metal (ion) transporter (dmt1) by proteasomal degradation. *Biometals*. 2012;25(4):787–793.

67- Nagabhushana A, Chalasani ML, Jain N, *et al*. Regulation of endocytic trafficking of transferrin receptor by optineurin and its impairment by a glaucoma-associated mutant. *BMC Cell Biol*. 2010;11:4.

68- Xiong Q, Li X, Li W, *et al*. *WDR45* mutation impairs the autophagic degradation of transferrin receptor and promotes ferroptosis. *Front Mol Biosci.* 2021;8:645831.

69- Zuyderhoudt FJ, Sindram JW, Marx JM, Jorning GA, Goo J. The amount of ferritin and hemosiderin in the livers of patients with iron-loading diseases. *Hepatol.* 1983;3(2): 232-235.

70- Asano T, Komatsu M, Yamaguchi-Iwai Y, Ishikawa F, Mizushima N, Iwai K. Distinct mechanisms of ferritin delivery to lysosomes in iron-depleted and ion-replete cells. *Mol Cell Biol.* 2011;31(10):2040–2052.

71- Saito H, Tomita A, Ohashi H, Maeda H, Hayashi H, Naoe T. Determination of ferritin and hemosiderin iron in patients with normal iron stores and iron overload by serum ferritin kinetics. *Nagoya J Med Sci*. 2012;74 :39-49.

72- Bridges KR. Ascorbic acid inhibits lysosomal autophagy of ferritin. *J. Biol. Chem*. 1992;262(30) :14773-14778.

73- Ramey G, Deschemin JC, Durel B, Canonne-Hergaux F, Nicolas G, Vaulont S. Hepcidin targets ferroportin for degradation in hepatocytes. *Haematologica* 2010; 95(3):501-504.

74- Diaz V, Gammella E, Racalcatti S, *et al*. Liver iron modulates hepcidin expression during chronically elevated erythropoiesis in mice. *Hepatology*. 2013;58(6):2122-2132.

75- Sabelli M, Montosi G, Garuti C, et al. Human macrophage ferroportin biology and the basis for the ferroportin disease. *Hepatology.* 2017;65(5):1512-1525.

76- Aboud S, Haile DJ. A novel mammalian iron-regulated protein involved in intracellular iron metabolism. *J Biol Chem.* 2000;275(26):19906–19912.

77- D'Anna MC, Veuthey TV, Roque ME. Immunolocalization of ferroportin in healthy and anemic mice. *J Histochem Cytochem.* 2009;57(1):9-16.

78- Delaby C, Pilard N, Puy H, Canonne-Hergaux F. Sequential regulation of ferroportin expression after erythrophagocytosis in murine macrophages: early mRNA induction by haem, followed by iron-dependent protein expression. *Biochem J.* 2008;411(1):123–13.

79- Winn K, Volk KM, Hasty AH. Regulation of tissue iron homeostasis: the macrophage “ferrostat ”. *JCI Insight* 2020;5(2)e132964.

TABLE Table 1. Peripheral red blood cell indices and iron parameters. Red blood cell (RBC) counts, hemoglobin (Hb) levels, hematocrit (HCT) levels, mean corpuscular volume (MCV), bilirubin, Epo, serum iron, total iron binding capacity (TIBC), transferrin saturation (TS), and serum ferritin (SF) in *LysM-Atg5*$^{-/-}$ and WT mice.

Genotype	RBC $10^6/mm^3$	Hb g/dL	HCT %	MCV fL	Bilirubin mg/dL	EPO pg/mL	Serum iron µg/dL	TIBC µg/dL	TS %	SF pg/mL
wt/wt	8.55±0.97	13.62±0.65	43.65±2.84	46.46±1.10	0.28±0.19	733.71±256	275.9±90.62	345±92	49.59±8.8	119.2±28.5
LysM-Atg5$^{-/-}$	9.09±0.61	13.90±0.74	42.05±2.76	46.31±1.09	0.2±0.13	726±372	321.4±115.31	322±48	57.28±16.8	123.6±38.4
p	0.66	0.58	0.44	0.91	0.39	0.97	0.0004	0.34	0.0064	0.96

FIGURE LEGENDS

Figure 1. *LysM-Atg5*$^{-/-}$ mice had normal hepatic histology but mild fibrosis.

(A) Histogram of the mean and standard error values with dot plots of liver weight normalized to body weight; n = 14 to 15 in each group. (B) Representative liver anatomy of *LysM-Atg5*$^{-/-}$ and WT mice. Immunofluorescence of liver sections stained with a PE-conjugated anti-F4/80 antibody (red) and DAPI (blue) for nuclear staining showing a similar Kupffer cell distribution (Leica fluorescence microcopy imaging, original magnification 20x; Scale bars, 20 μm). Liver sections stained with hematoxylin/eosin (H&E) and Sirius red with Fast green counterstaining (NanoZoomer scan imaging, original magnification 20x; Scale bars, 50 μm); Sirius red^{+} areas of collagen (red) are indicative of mild liver fibrosis in *LysM-Atg5*$^{-/-}$ mouse livers. Histological staining panels are representative of *LysM-Atg5*$^{-/-}$ and WT mice (n= 8 per group). (C) Histogram of the mean and standard error values with dot plots of serum AST levels (n=12-15 in each group). *p < .05

Figure 2. Increased erythropoiesis in *LysM-Atg5*$^{-/-}$ mice.

(A) Representative example of *LysM-Atg5*$^{-/-}$ and WT mouse spleens and spleen weight-to-body weight (%) ratios. Data are presented as histograms of the mean and standard error values, with individual measurements; n= 14-15 in each group. ****p<10^{-4}. (B) Macrophage localization and cell count. Immunofluorescence with a PE-conjugated anti-F4/80 antibody for macrophage staining (red) and DAPI (blue) for nuclear staining; and flow cytometric analysis results depicted as dot plot-type histograms (mean values and standard errors, n=6) showing the F4/80^{+}/CD11b^{-} macrophage and CD11b^{+}/F4/80^{-} monocyte populations in the spleens of *LysM-Atg5*$^{-/-}$ and WT mice. Leica fluorescence microcopy imaging, original magnification 20x; Scale bars, 20 μm; The gating strategy is shown in supplemental Figure 3A. (C) Spleen (**i**) and bone marrow (**ii**) histology and blood cell analysis (**iii**) with flow cytometry plots showing erythroid lineage cells from *LysM-Atg5*$^{-/-}$ and WT mice. **i**, H&E-stained sections of spleen tissue WP, white pulp; RP, red pulp. NanoZoomer scan imaging, original magnification 5x; Scale bars 200 μm, representative from n = 10 per group. The insets in the spleen panels show enlarged images of the boxed regions (original images 40x ; Scale bars, 20 μm) showing brown hemosiderin deposits in WT mice and erythroblastic islands consisting of a central nurse macrophage surrounded by a ring of developing red blood cell precursors in *LysM-Atg5*$^{-/-}$ mice. **ii**, H&E-stained bone sections. Leica microcopy imaging, original magnification 20x; Scale bars 20 μm, representative from n = 3 per group. **iii**, Peripheral blood smears stained with May-

Grunwald-Giemsa stain ; the arrows indicate hematoxylin blue-stained reticulocytes (NanoZoomer scan imaging, original magnification 20x; Scale bars, 20 μm). Representative flow cytometry plots for spleen, bone marrow and blood showing erythroid precursors based on CD71 and Ter119 markers used to separate the erythroid progenitors. The gating strategy is shown in supplemental Figure 3A. The relative percentages of cells in stages I-IV of erythropoiesis with stage I single-positive $CD71^{+}$ $Ter119^{-}$ early-stage proerythroblasts (region I), stage II double-positive $CD71^{+}$ $Ter119^{+}$ late-stage basophilic erythroblasts (region II), $CD71^{low}$ $Ter119^{+}$ polychromatic and orthochromatic erythroblasts (regions III and IV) and single-positive $CD71^{-}$ $Ter119^{+}$ $CD11b^{+}$ (region IV) in *LysM-Atg5*$^{-/-}$ and WT mice are indicated. Representative histograms of flow cytometry from n = 8-10 per group are shown in supplemental Figure 3B.

Figure 3. *LysM-Atg5*$^{-/-}$ mice have splenic and enterocytic iron depletion, ferroportin membrane localization and body iron overload.

(A) Histological examination of nonheme iron deposits in the spleen, duodenum and liver in *LysM-Atg5*$^{-/-}$ and WT mice. Nonheme iron deposition was visualized by Perl's staining (blue) of spleen and duodenum sections and after DAB enhancement (brown) for liver sections (representative images are shown from n = 12 per group; NanoZoomer scan imaging; original magnification, 10x for spleen and liver and 20x for duodenum; scale bars, 100 μm for spleen and liver and 40 μm for duodenum; enlarged inset images, 40x; scale bars, 20 μm). The duodenum images show the proximal (top) part where food was no longer in transit and the more distal (down) part where food was in transit. Iron was localized in the apical compartment of WT enterocytes in both parts of the duodenum, whereas in *LysM-Atg5*$^{-/-}$ enterocytes no iron was seen in the proximal duodenum but iron was localized in both the apical and basal compartments of in the distal duodenum. Enlarged liver images show Kupffer cells stained for iron in WT mice and hepatocyte staining in *LysM-Atg5*$^{-/-}$ mice. (B) Tissue iron content in the spleen (**i top**) and liver (**iii top**) in *LysM-Atg5*$^{-/-}$ and wild-type mice, as determined by a ferrozine assay and reported as ng of iron per mg of dried tissue. Data are presented as histograms of the mean and standard error values with dot plots (n = 10 in each group). Representative Fpn immunoblotting from duodenal membrane protein extracts (**ii top**) from *LysM-Atg5*$^{-/-}$ and WT mice (n = 2 samples per genotype are shown from 6 mice). Representative staining of ferric iron loaded in ferritin (Fe-Ft) and immunoblotting of ferritin H (Ft-H) in the spleen (**i bottom**), duodenal (**ii bottom**), and liver (**iii bottom**) extracts. For ferric iron loaded ferritin, 25 ng of native proteins from cytosolic lysates was loaded in each lane of a nondenaturing PAGE gel,

and after electrophoresis, the gel was directly stained with Perl's staining solution and enhanced with DAB. The gel was then immunoblotted for Ft-H as a control for the band specificity. Representative images from 4 experiments are shown. For Ft-H western blot 25 ng of cytoplasmic extracts was loaded on a denaturing PAGE gel and Gapdh is shown as the loading control. Densitometric analysis was performed on the immunoblot shown as well as on immunoblots with lysates from 3 additional *LysM-Atg5*$^{-/-}$ and WT mice; after normalization to Gapdh in each lane, *LysMAtg5*$^{-/-}$ results were normalized to the WT control group average. Data are presented as means ± standard errors. (C) Calcein fluorescence quenching assay in spleen cells from *LysM-Atg5*$^{-/-}$ and WT mice for measurement of the labile iron pool. Immediately after recovery, cells dissociated from the spleen were stained simultaneously with calcein (CA-AM) and anti-mouse PerCP-conjugated CD11b and PE-Cy7-conjugated F4/80 antibodies and were then analyzed by flow cytometry. Gates were set on FSC, CD45 and TCRβ. Representative calcein fluorescence profiles of unstained cells (FMO-calcein) and calcein-AM-stained cells (WT and *LysM-Atg5*$^{-/-}$) with respect to cell markers are shown, and histograms with the mean and standard error values from 3 independent experiments are shown as dot-plots. **D.** Detection of ferroportin by immunofluorescence in spleen tissus, isolated cells from the spleen, and proximal duodenal villi from *LysM-Atg5*$^{-/-}$ and WT mice. Representative images are composites from ferroportin (red) and 4′,6-diamidino-2-phenylindole (DAPI)-stained nuclei (blue) (n= 4 animals per group; for spleen and spleen cell smear: Leica fluorescence microcopy imaging; original magnification 20x; scale bars, 20 µm; enlarged inset images, magnification 100x; scale bars, 5 µm; for liver: Zeiss inverted microscopy imaging; original magnification, 20x ; scale bars, 20 µm). *p < .05, ****p<10^{-4}. MFI, mean fluorescence intensity.

Figure 4. *Hamp1* expression in *LysM-Atg5*$^{-/-}$ mice

(Ai) Liver *Hamp1*, *Id1* and *Fga* mRNA levels (relative to *Gapdh*) expressed as -ΔCt values and correlation of *Hamp1* and *Id1* mRNA levels. n = 8 per group. (Aii) Ratio of liver *Hamp1* mRNA levels to hepatic iron content. (Aiii) Detection of hepcidin by immunofluorescence in liver tissue, from *LysM-Atg5*$^{-/-}$ and WT mice. Representative images are composites from hepcidin (red) and 4′,6-diamidino-2-phenylindole (DAPI)-stained nuclei (blue) (n = 4 animals per group; Leica fluorescence microcopy imaging; acquisition time, 3.000 ms, original magnification, 10x; scale bars, 50 µm. (B) Dot blotting of serum hepcidin from *LysM-Atg5*$^{-/-}$ and WT mice. 5 µL of serum samples were spotted. Three samples per genotype and controls of WT mice stimulated with LPS (5 µg/25 g) 24 hours prior necropsy are shown (control dot blots of 10% milk, serum

from WT mice fed iron-replete, iron-deficient, and iron-rich diets are shown in Supplemental figure 4 D; densitometric analysis was performed on n = 6 samples per group, and P values are given). (Ci) Spleen *Hamp1, Id1* and *Fga* mRNA levels (relative to *Gapdh*) expressed as -ΔCt values (values are the mean of n = 6 experiments). Data are presented as means and standard errors (n = 6 per group). (Cii) Detection of hepcidin by immunofluorescence in spleen from *LysM-Atg5*$^{-/-}$ and WT mice. Representative images are composites from hepcidin (red) and DAPI-stained nuclei (blue) (n = 4 animals per group; Leica fluorescence microcopy imaging, acquisition time, 100 ms; original magnification, 10x, scale bars, 50 μm). (D) Detection of hepcidin by immunofluorescence in duodenum from *LysM-Atg5*$^{-/-}$ and WT mice. Representative images are composites from hepcidin (red) and DAPI-stained nuclei (blue) (n = 3 animals per group; Zeiss inverted microscopy imaging; original magnification, 10x ; scale bars, 20 μm). Hepcidin protein was detected using a specifc rabbit anti-hepcicin-25 antibody.[58] *p <.05, **p < .01, ***p<.001, ****p<10^{-4}. RP, red pulp; WP, white pulp.

Figure 5. Autophagy deficient BMDMs can form ferric-ferritin and have high ferroportin level.

(A) Protein expression (i) and ferric ferritin (ii) in nontreated or treated BMDMs with FAC, holo-TF, or oRBCs. BMDMs plated (10^5) onto 96-wells were treated for 16 h either with FAC (100 μM), holo-TF (30 μM) or oRBCs (5 oRBC:1 cells). (Ai) Immunoblotting of Atg5 (Atg5/Atg12 complex is shown), p62, Fpn, Ft-H, HO-1 and β-actin as the loading controls. (Aii) Staining of ferric iron loaded in ferritin on native polyacrylamide gel electrophoresis (PAGE) gels in BMDMs after the indicated treatments; 25 ng of native proteins from cytosolic lysates was loaded in each lane of a nondenaturing PAGE gel, and after electrophoresis the gel was directly stained with Perl's staining solution and enhanced with DAB (representative images from n = 3 experiments are shown; quantitative analysis of the western blots is given in supplemental Table 3). (B) Calcein quenching assay for labile iron pool (LIP) measurement, ROS levels, and membrane TfR1 expression. Cells were plated (10^5) in 96-wells plates and treated for 16 h with FAC (100 μM), holo-TF (30 μM) or oRBCs (oRBCs to cells, 5:1). For intracellular LIP measurement based on calcein quenching and the ROS assay, after addition of calcein-AM (calcein quenching assay) or H_2DCFDA (ROS assay) fluorescence intensity was measured (representative analysis of n = 3 independent experiments is shown). For calcein, the mean fluorescence intensity of treated cells was normalized to that of untreated control cells. ROS production is represented as the percentage relative to that in untreated control cells. For evaluation of TfR1 membrane expression, cells were incubated with BV510 anti-CD45,

phycoerythrin-Cy7 F4/80 and eFluor450 CD71 anti-mouse antibodies and analyzed by flow cytometry.

Figure 6. Erythrophagocytosis activates autophagy in BMDMs, and autophagy deficiency in BMDMs abrogated ferroportin degradation.

(A) Expression kinetics in BMDMs treated with oRBCs. *Atg5*$^{-/-}$ and WT BMDMs were incubated with oRBCs (oRBCs to cells, 5:1) for the indicated times. Western blot analysis of Hif2α, p62, LC3 from total protein extracts and Fpn from membrane extracts, and β-actin as control in BMDMs from *LysM-Atg5*$^{-/-}$ and WT mice incubated with oRBCs (5 oRBC:1 cell) for the indicated times. After treatment with oRBCs, protein was extracted from BMDMs for western blot analysis (representative analysis of n = 3 independent experiments is shown; quantitative analysis of the western blots is given in supplemental Table 4). (B) Kinetics of *Hmox1*, *Fpn* and *Hamp1* mRNA expression in BMDMs treated with oRBCs. Representative mRNA fold changes (relative to *Gapdh*) expressed as -ΔΔCt values (n = 3 replicates). Data are presented as means and standard errors. (C) Iron loading and ferroportin localization in BMDMs from *LysM-Atg5*$^{-/-}$ and WT mice treated with oRBCs. (Ci) Representative images of Perl's/DAB iron stained BMDMs (NanoZoom scan imaging; original magnification, 40x). BMDMs cultured on slides incubated for the indicated times after treatment with oRBCs (oRBC to cells 5:1) were fixed with paraformaldehyde for immunostaining or with methanol for Perl's staining followed by DAB enhancement. (Cii) Detection of ferroportin by immunofluorescence in BMDMs from *LysM-Atg5*$^{-/-}$ and WT mice. Images are composites of ferroportin (red) and 4′,6-diamidino-2-phenylindole (DAPI)-stained nuclei (blue) (Leica fluorescence microcopy imaging; original magnification, 100x; representative images shown are from n = 4 independent experiments). (D) Immunofluorescence colocalization of ferroportin in BMDMs from WT mice treated with oRBCs. WT BMDMs were double-labeled with a rabbit anti-Fpn antibody and Alexa Fluor 488-conjugated secondary donkey anti-rabbit immunoglobulin (IgG red), followed by rabbit anti-Atg5 antibody and TRITC-conjugated goat secondary anti-rabbit IgG (green). Cell nuclei were stained with DAPI (blue). Erythrophagocytosis resulted in colocalization of ferroportin and Atg5 in erythrophagocytic BMDMs at 8h to 16h (Leica fluorescence microcopy imaging; original magnification, 40x; representative images shown are from n = 2 independent experiments). (E) Immunofluorescence colocalization of ferroportin and hepcidin in BMDMs from *LysM-Atg5*$^{-/-}$ and WT mice treated with oRBCs. WT and *Atg5*$^{-/-}$ BMDMs were double-labeled with a rabbit anti-ferroportin antibody and Alexa Fluor 488-conjugated secondary donkey anti-rabbit IgG (red), followed by rabbit anti-hepcidin antibody[58] and TRITC-

conjugated secondary goat anti-rabbit IgG (green). Cell nuclei were stained with DAPI (blue). Erythrophagocytosis resulted in colocalization of ferroportin and hepcidin in WT cells at 12h and *Atg5*$^{-/-}$ cells at 16h (Leica fluorescence microcopy imaging; original magnification, 40x; representative images shown are from n = 2 independent experiments). *p<.05, **p<.01, ***p<.001, ****p<10^{-4}.

Figure 7. Schematic figure of key similarities and differences between WT and *LysM-Atg5*$^{-/-}$ mice. (A) Wild-type mice. Erythrocytes are phagocytosed by macrophages. Macrophages efficiently recycle phagocytosed iron to transferrin in the circulation and with the help of autophagy the excess iron is stored in hemosiderin. A small amount of iron uptake by enterocytes is released from enterocytes, most is stored in ferritin. Tranferrin-bound iron is carried to bone marrow. Iron is incorporated into newly formed erythrocytes within the bone marrow. Hepcidin produced from hepatocytes and macrophages control cell iron release. (B) *LysM-Atg5*$^{-/-}$ mice. Erythrocytes are phagocytosed by macrophages. Macrophages efficiently recycle phagocytosed iron to transferrin in the circulation but without functional autophagy ferroportin from red blood cells can not be sufficiently degraded and the excess iron can not be stored in hemosiderin. High iron release from macrophages decrease hepcidin expression. Large amount of iron is released from macrophages and absorbed from enterocytes. Tranferrin-bound iron is carried in excess to bone marrow and extramedullary sites of erythropoiesis. Iron is incorporated into an excess of newly formed erythrocytes. ATG: autophagy. Dashed lines indicate iron transit.

Figure 1

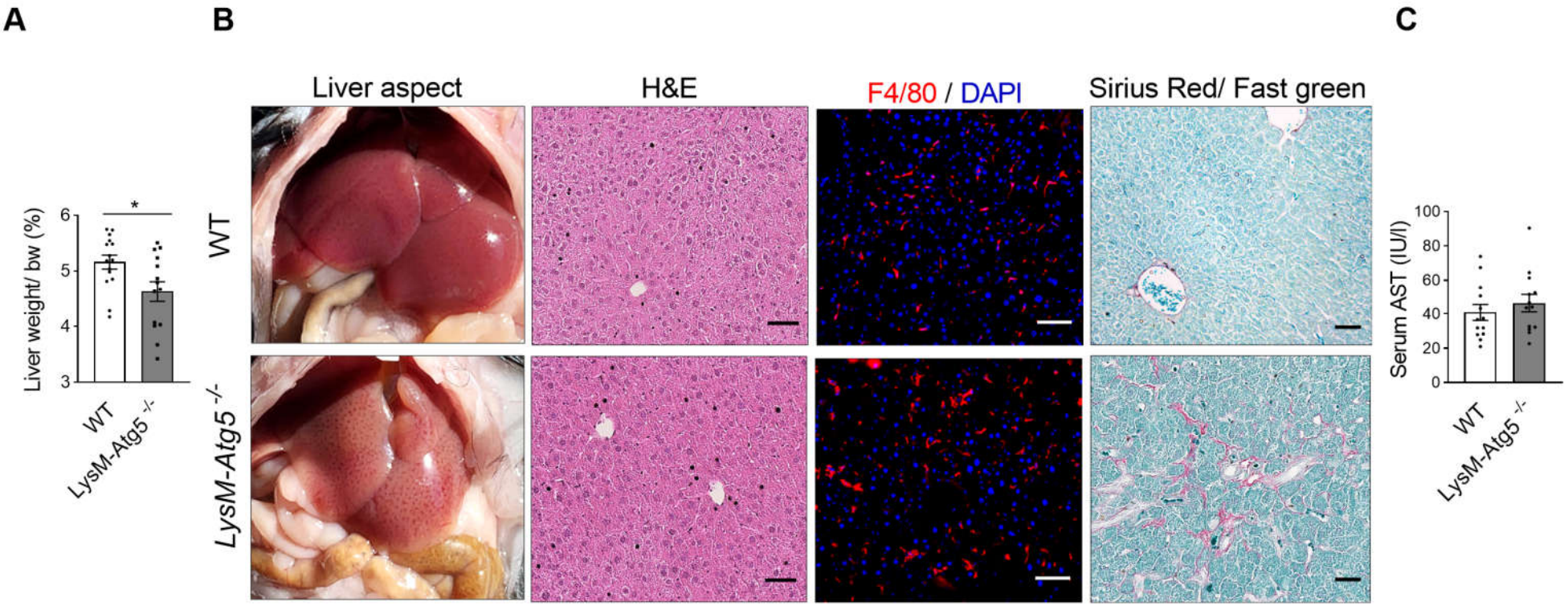
A
B
C
Liver aspect
H&E
F4/80 / DAPI
Sirius Red/ Fast green
WT
LysM-Atg5 -/-
Liver weight/ bw (%)
6
5
4
3
*
WT
LysM-Atg5 -/-
Serum AST (IU/l)
100
80
60
40
20
0
WT
LysM-Atg5 -/-

Figure 2

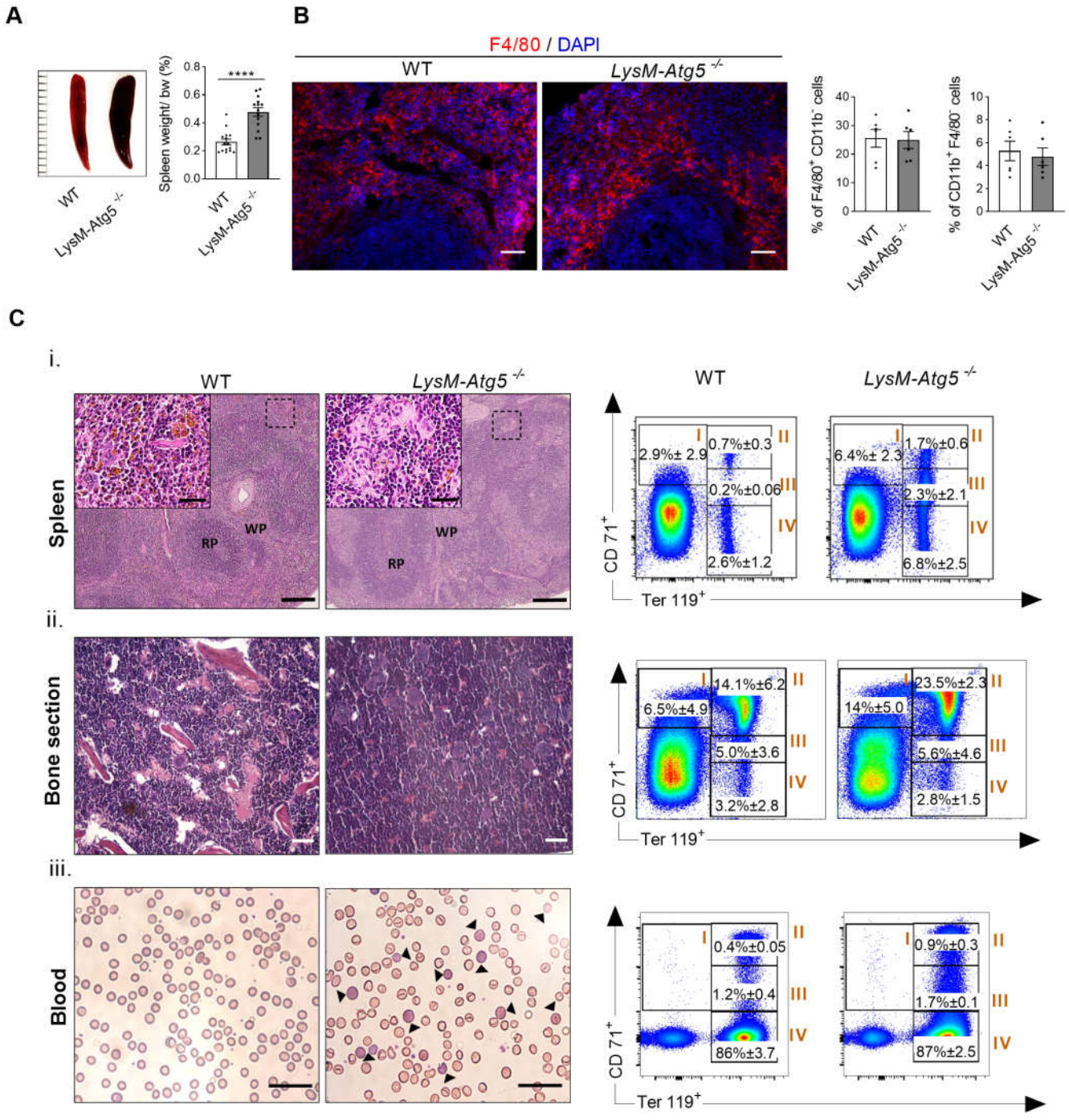
A
WT
LysM-Atg5 -/-
Spleen weight/ bw (%)
****
B
F4/80 / DAPI
WT
LysM-Atg5 -/-
% of F4/80+ CD11b- cells
% of CD11b+ F4/80- cells
C
i.
ii.
iii.
Spleen
Bone section
Blood
WP
RP
CD 71+
Ter 119+
2.9%± 2.9
0.7%±0.3
0.2%±0.06
2.6%±1.2
6.4%± 2.3
1.7%±0.6
2.3%±2.1
6.8%±2.5
6.5%±4.9
14.1%±6.2
5.0%±3.6
3.2%±2.8
14%±5.0
23.5%±2.3
5.6%±4.6
2.8%±1.5
0.4%±0.05
1.2%±0.4
86%±3.7
0.9%±0.3
1.7%±0.1
87%±2.5

Figure 3

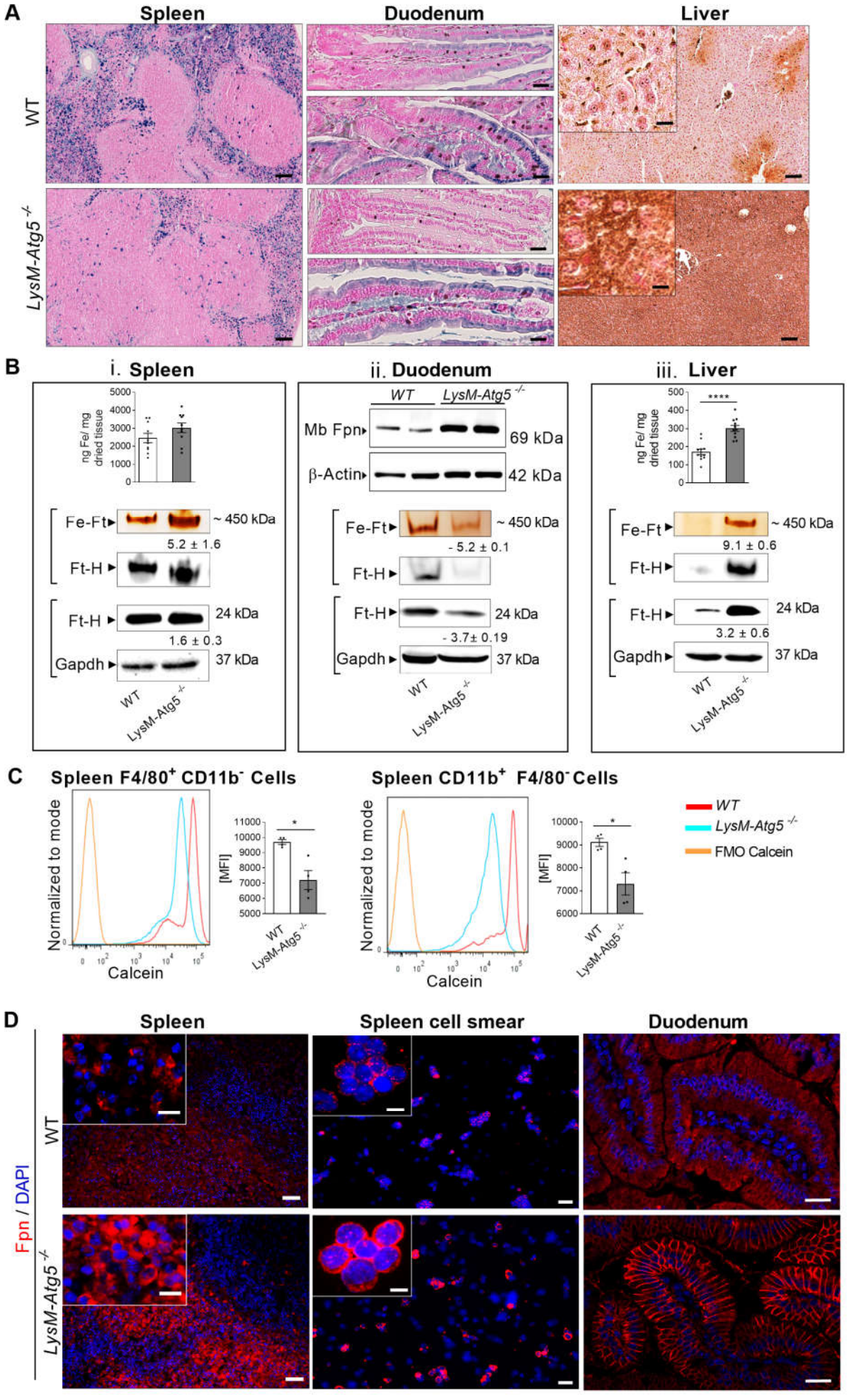
A
Spleen
Duodenum
Liver
WT
LysM-Atg5 -/-
B
i. Spleen
ii. Duodenum
iii. Liver
ng Fe/ mg dried tissue
WT
LysM-Atg5 -/-
Mb Fpn
69 kDa
β-Actin
42 kDa
Fe-Ft
~ 450 kDa
5.2 ± 1.6
- 5.2 ± 0.1
9.1 ± 0.6
Ft-H
24 kDa
1.6 ± 0.3
- 3.7± 0.19
3.2 ± 0.6
Gapdh
37 kDa
****
C
Spleen F4/80+ CD11b- Cells
Spleen CD11b+ F4/80- Cells
Normalized to mode
Calcein
[MFI]
*
WT
LysM-Atg5 -/-
FMO Calcein
D
Spleen
Spleen cell smear
Duodenum
WT
LysM-Atg5 -/-
Fpn / DAPI

Figure 4

A Liver

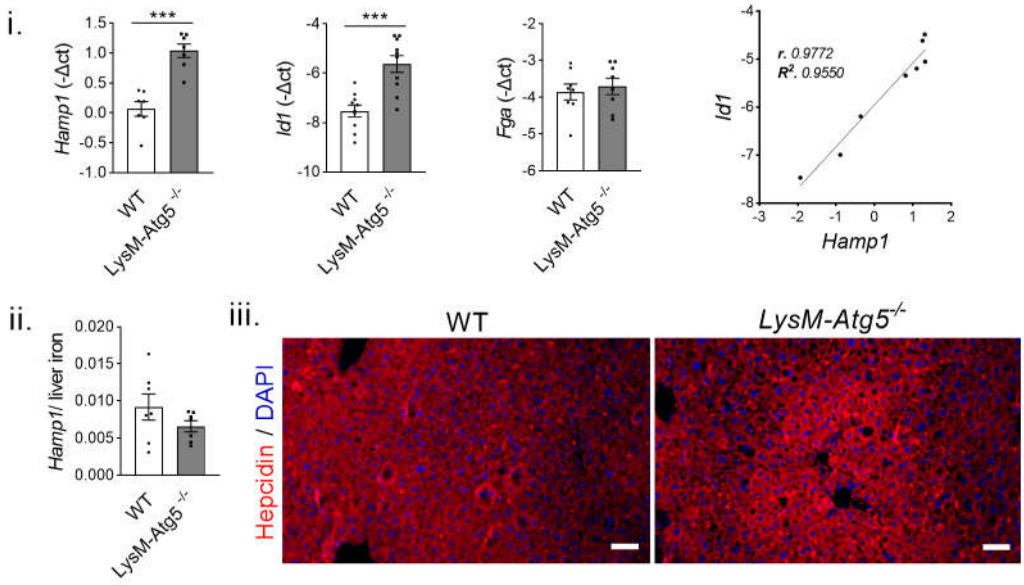

B Serum

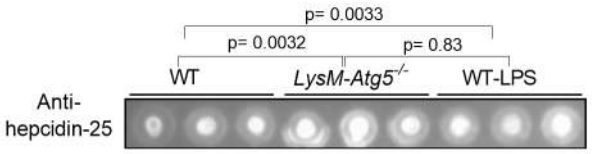

C Spleen

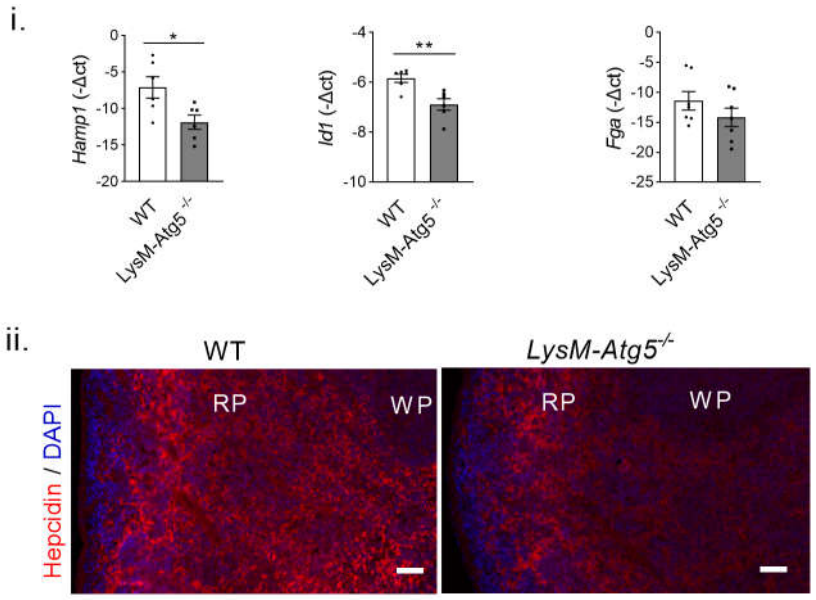

D Duodenum

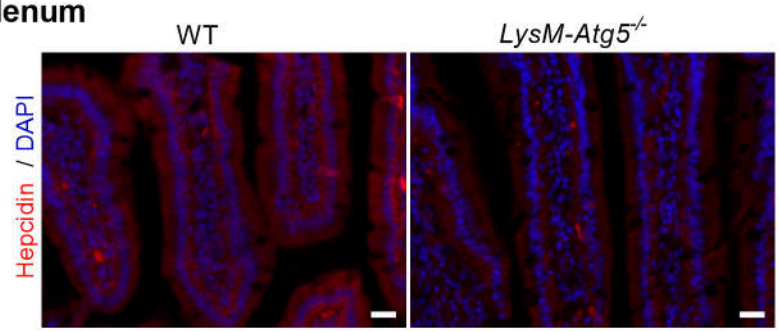

Figure 5

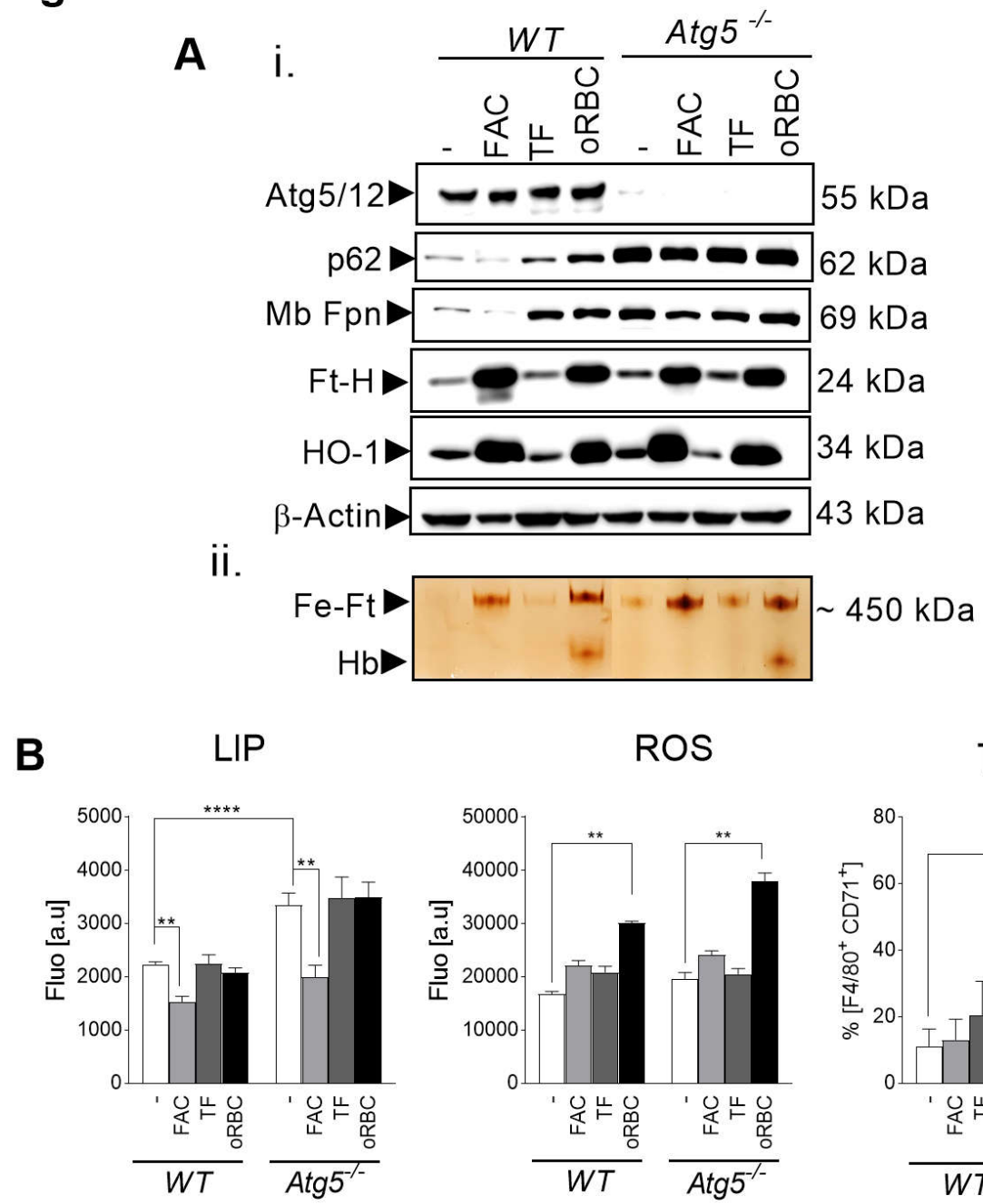
A
i.
WT
Atg5 -/-
-
FAC
TF
oRBC
Atg5/12
55 kDa
p62
62 kDa
Mb Fpn
69 kDa
Ft-H
24 kDa
HO-1
34 kDa
β-Actin
43 kDa
ii.
Fe-Ft
Hb
~ 450 kDa
B
LIP
ROS
TfR1
Fluo [a.u]
% [F4/80+ CD71+]
WT
Atg5-/-

Figure 6

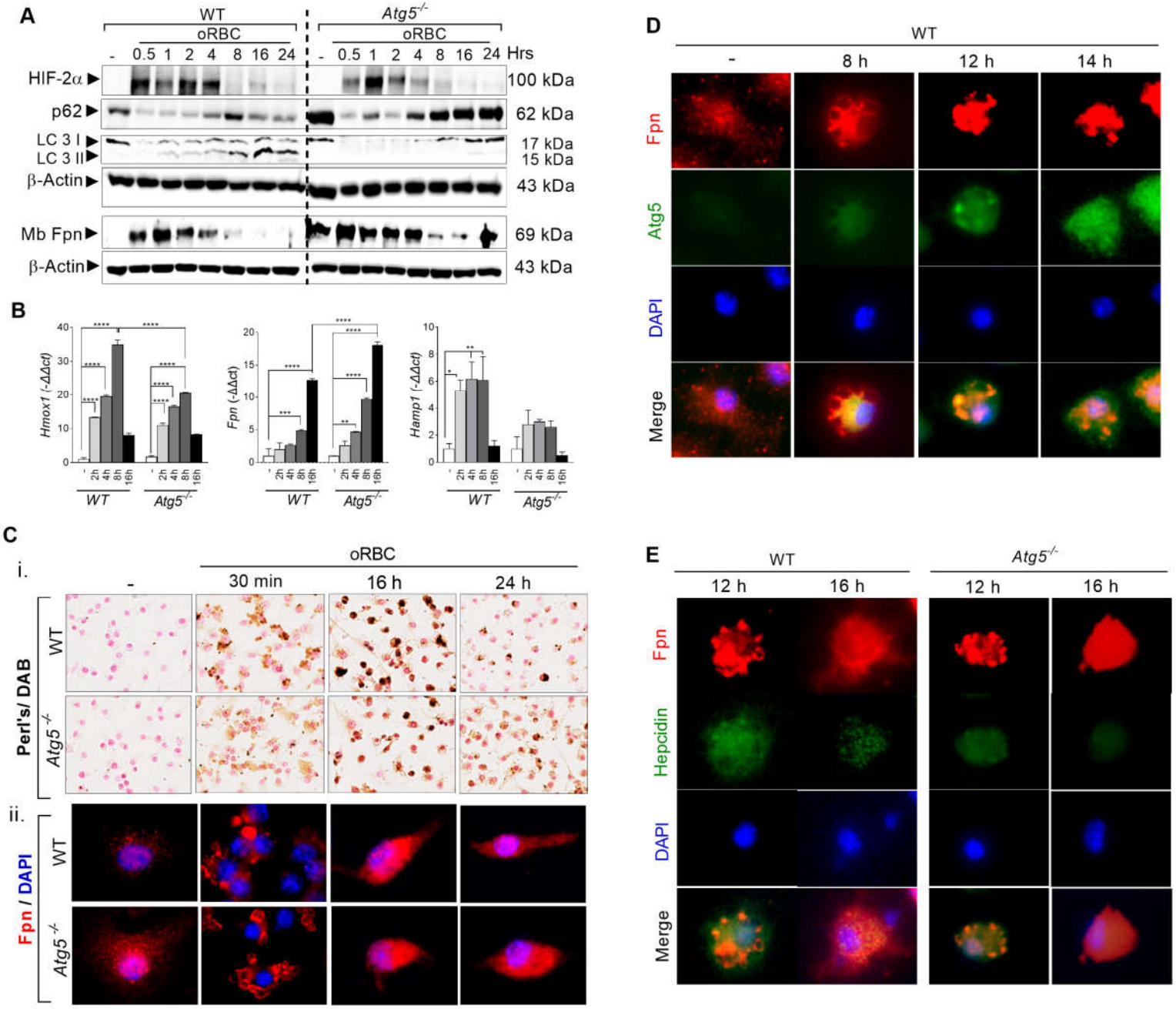
A
WT
oRBC
Atg5-/-
oRBC
- 0.5 1 2 4 8 16 24 Hrs
- 0.5 1 2 4 8 16 24
HIF-2α
p62
LC 3 I
LC 3 II
β-Actin
Mb Fpn
β-Actin
100 kDa
62 kDa
17 kDa
15 kDa
43 kDa
69 kDa
43 kDa
B
Hmox1 (-ΔΔct)
Fpn (-ΔΔct)
Hamp1 (-ΔΔct)
WT
Atg5-/-
C
i.
oRBC
-
30 min
16 h
24 h
Perl's/ DAB
WT
Atg5 -/-
ii.
Fpn / DAPI
WT
Atg5 -/-
D
WT
-
8 h
12 h
14 h
Fpn
Atg5
DAPI
Merge
E
WT
Atg5-/-
12 h
16 h
12 h
16 h
Fpn
Hepcidin
DAPI
Merge

Figure 7

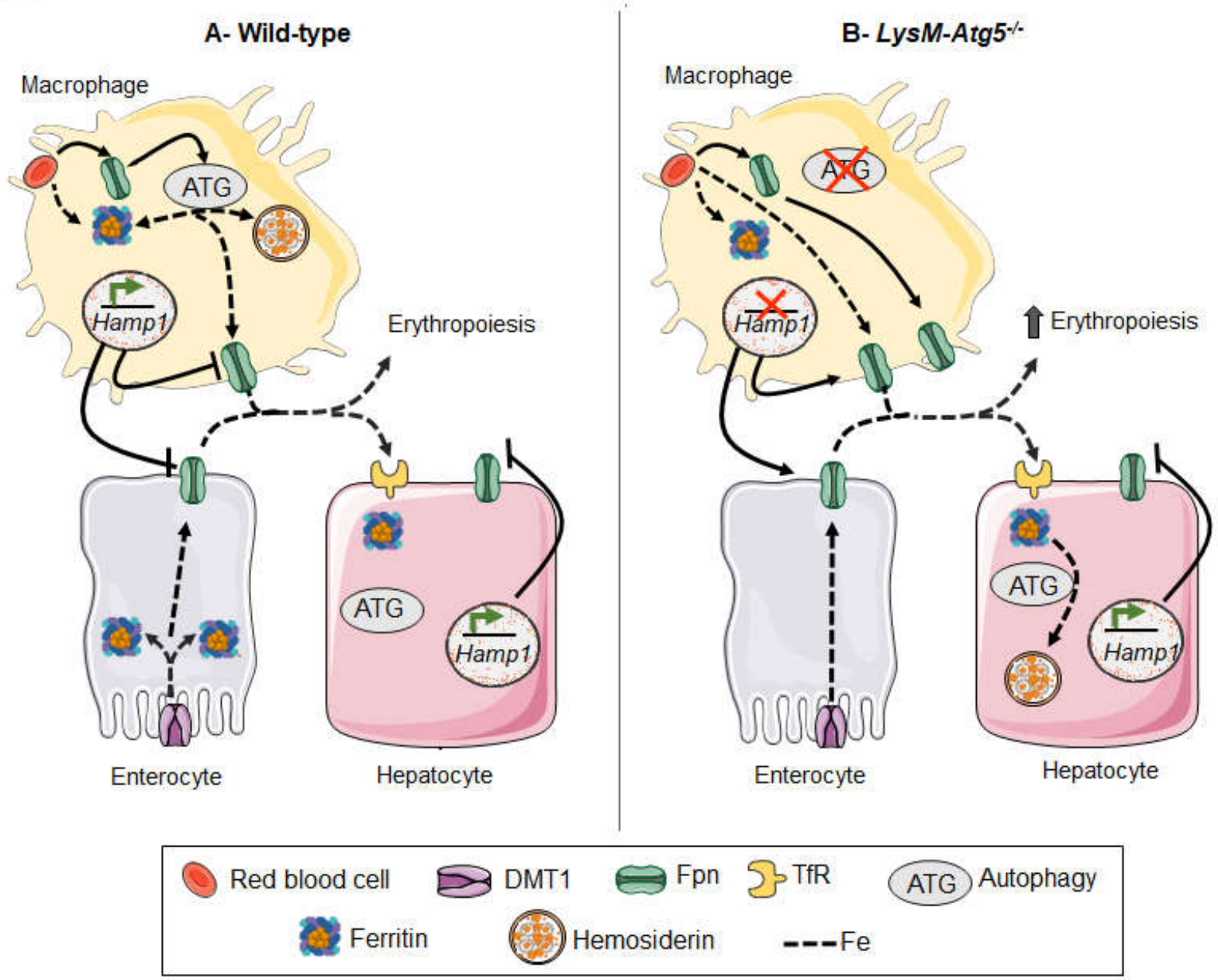
A- Wild-type
Macrophage
ATG
Hamp1
Erythropoiesis
ATG
Hamp1
Enterocyte
Hepatocyte
B- LysM-Atg5-/-
Macrophage
ATG
Hamp1
Erythropoiesis
ATG
Hamp1
Enterocyte
Hepatocyte
Red blood cell
DMT1
Fpn
TfR
ATG
Autophagy
Ferritin
Hemosiderin
Fe

SUPPLEMENTAL METHODS

Animals

Conditional mutant mice on a C57BL/6J background lacking the autophagy-related 5 gene (*Atg*5) in myeloid lineage cells, including monocytes, mature macrophages and granulocytes, were generated by crossing the Atg5 (autophagy gene 5) floxed ($Atg5^{fl/fl}$) mice [$Atg5^{tm1Myok}$, Hara *et al*. 2006] with *lysozyme M cre* (*LysM cre*) transgenic strain [Clausen *et al*. 1999] and then breeding $Atg5^{fl/+}$ *LysM Cre*. The mice referred to herein as *LysM-*$Atg5^{-/-}$ mice carried floxed alleles of *Atg5* and one copy of the *lysozyme M Cre* transgene. Cre-negative floxed ($Atg5^{fl/fl}$) littermate mice were used as wild-type controls. Mice were routinely typed by PCR from DNA extracted from tails (supplement Table 1 for primers). Both sexes were analyzed and, unless specified, the results were similar. The specificity and efficiency of tissue-specific recombination was checked by Atg5 immunofluorescence analysis in tissues and BMDMs. Mice were housed under specific pathogen-free conditions in our animal facility at the Transgenose Institute (UAR44 TAAM CNRS, Orléans, France) and had access to chow and water ad libitum. Mice were fed a standard commercial diet (R03 from Scientific Animal Food & Engineering; Augy, France) with a normal iron content of 250 mg iron/kg and were analyzed at 5 to 9 months old. All animal experiments complied with the French Government's animal experiment regulations and were approved by the National Ethics Committee for Animal Experimentation (CLE CCO 2020-23557).

Hematology, serum and iron analysis

Hematological parameters, serum and iron parameters, nonheme tissue iron content were analyzed as described previously [Agoro *et al*. 2017; Agoro *et al*. 2018]. Mice were anesthetized with isoflurane and blood was collected by retroorbital venipuncture in EDTA-containing tubes for plasma or in serum separator tubes (BD Biosciences, Franklin Lakes, NJ, USA). Hematological parameters were determined by using a SCIL Vet abc Plus^{+} hematometer (SCIL Animal Care Company, Altorf, France). The morphology of red blood cells was evaluated by blood smear staining with a Fast Quick May-Grunwald Giemsa kit (DiaPath kit, Martinengo, Italy). The serum iron concentration, unsaturated iron-binding capacity (UIBC), and transferrin saturation were determined by the standard ferrozine colorimetric method. Serum ferritin and serum erythropoietin (Epo) levels were quantified by enzyme immunoassay kits (Abnova, Taipei, Taïwan; R&D Systems, Minneapolis, MN, USA). Alanine aminotransferase (ALT) and aspartate aminotransferase (AST) levels were determined by a colorimetric method (Biolabo SAS, Maizy, France).

The nonheme tissue iron content was quantified by the ferrozine colorimetric method, and the results are reported as ng of iron per mg of dry tissue. Briefly, tissue samples were dried at 120°C for 16 h and were then weighed and dissolved in 1:1 sulfuric acid : nitric acid for 30 min at 90°C. After 1 mL of H_2O was added to the samples, 25 µL of extracted iron solution was reacted with ferrozine detection solution (10 mM ferrozine/32.6 mM L-ascorbic acid/50 mM Tris HCl (pH 4)) at room temperature for 30 min, and the absorbance was then measured at 562 nm. A standard $FeCl_3$ curve was used to calculate the iron concentration.

Histology

Tissue samples fixed in 4% phosphate buffered formalin, were processed for paraffin embedding and cross sectioning (5 µm). Bones were decalcified in 10% EDTA and 2.5% formalin in PBS (pH 7.4) for 20 days before paraffin embedding. Deparaffinized tissue sections were stained with hematoxylin/eosin (H&E), 0.1% sirius red solution/0.1% Fast Green in aqueous saturated picric acid. For assessment of ferric iron deposits, Perl's solution (3.7% hydrochloric acid and 5% potassium ferrocyanide/nuclear Fast Red) was used, with further enhancement with 3,3′-diaminobenzidine (DAB) (Sigma-Chemicals, St Louis, MO, USA) solution (0.025% DAB/0.12% H_2O_2 in PBS (pH7.4)) when indicated. Treatment with 0.5 mM H_2O_2 in PBS (pH7.4) for 1 hour was used before Perl's staining for iron oxidation when indicated. Snap frozen tissue cryosections were stained with Oil Red O (0.6% (w/v) in H_2O) and counterstained with hematoxylin. Histological images were acquired with a NanoZoomer NDP scan 1.0.9 scanner and imported into NDP view 2.0 software (Hamamatsu Photonics K.K., Japan).

Immunofluorescence microscopy

For immunofluorescence staining tissue sections were deparaffinized, cells isolated from spleen or bone marrow (as described above) and BMDMs (2.10^5 cells) plated on glass slides were fixed with 4% paraformaldehyde for 10 min. Fixed tissues or cells, for ferroportin staining were treated with 50 mM glycine/50 mM NH_4Cl for 15 min at room temperature, and for hepcidin staining were treated with 10 mM citric acid buffer, pH 6.0 / 0.05% Tween-20 at 90°C for 20 min. Slides were blocked with 10% horse serum/2% BSA/1 mM $CaCl_2$/1 mM $MgCl_2$ in PBS (pH7.4), then incubated with rabbit primary antibody overnight at 4°C, and then with a Alexa Fluor 488-conjugated goat secondary anti-rabbit IgG antibody for 2 h at room temperature. For double-staining, the fixed cells after blocking as described above were incubated with rabbit primary anti-ferroportin antibody, and secondary antibody Alexa-Fluor 568-conjugated donkey anti-rabbit IgG. Then, cells were blocked with 10% goat serum/2% BSA/1 mM $CaCl_2$/1 mM

$MgCl_2$ in PBS (pH7.4), incubated with a rabbit Atg5 or hepcidin primary antibody, and TRITC-conjugated goat secondary anti-rabbit IgG. For tissue, slides were treated with TrueBlack Lipofuscin Autofluorescence Quencher (Biotium, Fremont, CA, USA). Nuclei were stained with 4,6-diamidino-2-phenylindole (DAPI), and slides were washed and mounted (Fluoromount®, Thermo Fisher Scientific, Waltham, MA, USA). Parallel slides incubated without a primary antibody were used as negative controls. Immunofluorescence images were acquired by a Leica CTR6000 confocal microscope (Leica, Heidelberg, Germany) and imported into MetaMorph software (Molecular Devices, Downingtown, PA). For duodenum and liver, fluorescent microscopy images were acquired by a Zeiss Observer Z7 inverted microscope coupled with a Zeiss LSM 980 Airy Scan 2 device (Carl Zeiss Co. Ltd., Jena, Germany). Images were acquired using Zeiss ZEN blue 3.1 software (Carl Zeiss Co. Ltd., Jena, Germany).

Cytosolic lysate preparations and native ferritin analysis

For in-gel detection of ferric iron-loaded ferritin, fresh cytosolic native protein extracts (25 µg) of snap frozen tissues or BMDMs were prepared by homogenization in a 10 mM Tris (pH 7)/1 mM $MgCl_2$/1x protease inhibitor cocktail (Thermo Fisher Scientific) solution and incubated on ice for 10 min. After centrifugation at 25,000 x g, the supernatant was recovered as the cytosolic native protein fraction. The protein concentration was measured in a NanoDrop spectrophotometer at 280 nm. Native protein extracts were separated on nondenaturing 5% PAGE gels (30 mA for 1 h 30) at 4°C. The gels were stained in freshly prepared Perl's staining solution for 1 h at room temperature and further enhanced with DAB solution. After electroblotting, membranes were probed with a primary rabbit anti-ferritin antibody and secondary anti rabbit IgG as described below, to confirm that the bands were stained for ferric ferritin. In all experiments, only one band of high molecular weight (approximately 440 kDa) stained with Perl's stain/DAB was positive for anti-ferritin antibody. For normalization, Gapdh in its denatured (western blot) form was used.

Western and dot blot analyses

For western blotting, proteins were extracted from snap frozen tissues or BMDMs homogenized in denaturing lysis buffer (50 mM Tris pH 6.8, 2% SDS, 10% glycerol, and 5% β-mercaptoethanol), incubated for 1 h at room temperature and sonicated. For ferroportin protein preparation, after nondaturing cell lysis with 10 mM Tris (pH 7)/1 mM $MgCl_2$/1x protease inhibitor cocktail, proteins were extracted from membrane pellets by incubation with denaturing lysis buffer. The protein concentration was measured in a NanoDrop spectrophotometer at 280 nm. Samples were separated by SDS/PAGE, then electroblotted onto

membrane (Protran 0.2µm, Amersham). For serum dot blot, 5 µl of the samples were spotted onto a membrane strip. Membranes were blocked with a solution of Tris-buffered saline, 0.5% (v/v) Tween-20 (TBS-T) and 10% (w/v) skim milk for 2 h. Primary antibodies were diluted in TBS-T with 5% (w/v) skim milk and incubated overnight. After washes with TBS-T, incubation with the horseradish peroxidase-conjugated secondary anti-rabbit IgG antibody, further TBS-T washes, and incubation with a mouse anti-β-actin-HRP antibody for normalization, protein signals were detected using a chemiluminescence reagent (either ECL Prime Western Blotting Detection Reagent, GE Healthcare, Little Chalfont, Buckinghamshire, UK or SuperSignal™ West Femto Maximum Sensitivity Substrate, Thermo Fisher Scientific) and digitally imaged using Syngene Pxi4 System (Syngene, Cambridge, UK) Integrated Scientific Solutions). The band densitometric analysis results shown in this study are presented as the mean of three series of western blot analyses.

Fluorescence-activated cell sorting

A single-cell suspension of spleen cells was obtained by enzymatic digestion using liberase (125 µg/mL; Roche) and DNase I (1 mg/mL; Sigma-Aldrich) in a final volume of 1 mL of RPMI at 37°C for 30 min under agitation. The cells were then filtered through a 100 µm cell strainer, red blood cells were lysed (PharmLyse, BD Biosciences) (for erythrocyte staining, the lysis step was omitted), the cells were counted, and the concentrations were adjusted to 2.10^6 cells/mL. For bone marrow analysis, cells were harvested from femurs by injection of PBS; for BMDMs, 10^5 cells per well were plated in 96-well plates and treated as indicated. Blood cells were collected in EDTA and washed with PBS. Cells collected in PBS/5% FCS/2 mM EDTA were then incubated for 30 min at 4°C with Fc blocker and stained with a combination of fluorochrome-conjugated anti-mouse antibodies (supplemental Table 2). Erythroid precursors staining was performed as previously described in Koulnis *et al*. 2011.

For the calcein-AM assay, cells were collected in PBS and incubated for 15 min with 0.2 µM calcein acetoxymethyl ester (calcein-AM, Sigma Chemicals) probe. Calcein fluorescence was detected in the FITC channel. Fluorescence minus one controls were set up for all the antibodies used; 400.000 events were recorded for spleen, bone marrow, and red blood cell suspensions, and 150.000 events were recorded for BMDMs. Data were collected in a FACScan flow cytometer (BD FACS Canto^{TM}II, BD Biosciences) and analyzed with FlowJo software (FlowJo 7.6.5, Tree Star, Ashland, OR, USA).

RNA extraction and quantitative PCR analysis

Total RNA from tissue samples or cells was isolated by TRIzol (Invitrogen). Reverse transcription of 1 µg of total RNA was performed with a SuperScript III First-Strand Synthesis System (Life Technologies) in total volume of 20 µL. The mRNA levels of selected genes were measured using a QuantiTect SYBR Green PCR system (Qiagen) and an Aria Mx real time PCR system (Agilent Technologies, Santa Clara, CA, USA). *Hmox* and *Gapdh* quantitect primers from Qiagen were used, for the sequences of the primers of *Hamp1*, *Fpn* and *Ft-H,* see supplemental Table 1. For spleen and BMDM hepcidin qPCR a 12-cycle preamplification step was carried out. qRT-PCR was performed in triplicate, and target mRNA levels were normalized to that of the housekeeping gene *Gapdh* in the same RT sample. The -ΔCt ($\Delta C_t = C_{t\ target} - C_{t\ reference}$) method was used to calculate the relative steady state gene transcript levels in organs, and the $2^{-\Delta\Delta C_t}$ method ($\Delta\Delta C_t = \Delta C_{t\ treated} - \Delta C_{t\ control}$) was used to determine the fold changes in gene expression levels compared with untreated conditions for the *in vitro* BMDM experiments.

Bone marrow-derived macrophage generation and treatment

To obtain bone marrow derived macrophages (BMDMs), murine bone marrow cells harvested from femurs were differentiated into macrophages after culture for 6 days in Dulbecco's modified Eagle's medium (DMEM) supplemented with 2 mM L-glutamine, 25 mM HEPES, 20% heat-inactivated horse serum, 30% L929 cell supernatant containing macrophage-stimulating factor (M-CSF), and streptomycin/penicillin. Macrophages were then harvested in cold PBS, and plated at a density of 3 x 10^5 cells/cm^2 in DMEM supplemented with 2 mM L-glutamine, 25 mM HEPES, streptomycin/penicillin and 2% horse serum overnight. When indicated, cells were incubated with 100 µM ferric ammonium citrate (FAC), 30 µM holo-transferrin (holo-TF) (Sigma Chemicals), or opsonized red blood cells. Opsonized red blood cells were prepared as described in Kovtunovych *et al*. 2010. Briefly, fresh mouse blood collected in EDTA tubes and washed twice in Alsever's solution was incubated for 30 min at 4 °C with 0.25 mg/mL of rabbit anti-mouse red blood cell antibody (Rockland Immunochemicals, Limerick, PA, USA). Opsonization was checked by flow cytometry after labeling with Alexa Fluor 488-conjugated goat anti-rabbit IgG H + L secondary antibody (Invitrogen), and subsequent incubation with marcophages were performed at a red blood cell:macrophage ratio of 5:1.

After cell treatments, the cell count was assessed after 30 min of incubation with 20 µg/mL Hoechst 3342 (Invitrogen) at excitation/emission wavelengths 360 nm/460 nm. Mitochondrial

activity was assessed by an MTT assay. Cells were incubated for 2 h in culture medium containing 2.5 mg/ml 3-(4,5 dimethylthiazol-2-yl)2,5-diphenyltetrazolium bromide (MTT), and formazan was solubilized by the addition of 100 µL of 10% SDS in DMSO/0.6% acetic acid and incubation for 10 min. The absorbance of the formazan was measured at 610 nm. Lactate dehydrogenase (LDH) release was assessed with Cytotoxicity Assay Kit (Pierce™, Thermo Fisher Scientific) and glucose consumption was assessed with a glucose uptake colorimetric assay kit (Glucose GOD PAP, Biolabo, Maizy, France) according to the manufacturers' instructions.

The intracellular labile iron pool (LIP) was measured based on a calcein quenching assay in which the ability of labile iron to bind and quench the fluorescence of the cell-permeable chelator calcein acetoxymethyl ester (CA-AM) in a stochiometric manner. For the iron calcein quenching and ROS assays, cells were plated (10^5) in 96-well black-bottom plates and treated as indicated; after washing cells were incubated with 1 µM nonfluorescent calcein-AM for 15 min (calcein quenching assay) or 5 mM H_2DCFDA for 30 min (ROS assay) at 37°C and were then washed before measurment using 480 nm/530 nm and 490 nm/520 nm filter pairs, respectively, in a Fluoroskan Ascent microplate fluorometer (Thermo Scientific)

Statistical analysis

GraphPad Prism Software was used for statistical analyses. An unpaired Mann-Whitney test was used for comparisons between two independent groups. Correlations were evaluated using Spearman correlation analysis. One-way ANOVA with Tukey's post hoc test for pairwise comparisons was used for comparisons among more than two groups. Significance levels are indicated as * $p < 0.05$, ** $p < 0.01$, ***$p < 0.001$, ****$p<10^{-4}$.

SUPPLEMENTAL FIGURES

Supplemental Figure 1

A. Genotyping of *LysM-Atg5*$^{-/-}$ mice. Floxed mice which harbor exon 3 of the *Atg5* gene flanked by two loxP sites and are heterozygous for *lysozyme M cre* were genotyped by PCR. Gel electrophoresis shows the amplification of *Atg5* (upper gel) with WT *Atg5* allele (357 bp), *Atg5*^{fl} allele (700 bp), and *LysM* (lower gels) with the *LysM* allele (345 bp) and *LysM cre* allele (711 bp).

B. **Efficiency and tissue-specific recombination of *Atg5***. To monitore Cre-mediated recombination after *Atg5*$^{fl/fl}$ mice breading with *lysozyme M cre* mice, the endogenous Atg5 expression was analyzed by immunofluorescence in tissue sections and BMDMs. In wild-type mice, high Atg5 staining in macrophages of the red pulp of the spleen, hepatocytes (higher around the portal zone) and the kupffer cells of the liver, as well in BMDMs was observed. In *LysM-Atg5*$^{-/-}$ mice no staining was observed in the red pulp of the spleen, kupffer cells and BMDMs, while staining was observed in hepatocytes and scarce in the white pulp of the spleen. Representative images are composites of Atg5 (red) and DAPI-stained nuclei (blue) from 3 animals per group. Arrows indicate Kupffer cells. Zeiss fluorescence inverted microcopy imaging, original magnification 20x for spleen and liver, 40x for BMDMs.

C. Body weight of *LysM-Atg5*$^{-/-}$ and wild-type mice. Dot plot histogram of the mean and standard error values of the body weights of male (M) and female (F) mice 5-8 months old; n= 4-7 in each group. **p=0.01.

D. Myeloid cell counts in peripheral blood of *LysM-Atg5*$^{-/-}$ and wild-type mice. Dot plot histogram of the mean and standard error values of white blood cell (WBC) and monocyte (Mono), neutrophil (NP), eosinophil (EOS) counts in the peripheral blood of *LysM-Atg5*$^{-/-}$ mice and WT animals; n= 12 in each group.

Supplemental Figure 2. Analysis of liver damage.

A. Oil Red O staining of liver cryosections from *LysM-Atg5*$^{-/-}$ and wild-type mice. *LysM-Atg5*$^{-/-}$ section show lipid droplets (red). Leica micropcopy images, original magnification 20x; Scale bars, 20 μm.

B. **Analysis of liver inflammatory parameters in *LysM-Atg5*$^{-/-}$ and WT mice.** IL6 and TNFα cytokines and myeloperoxidase (MPO) expression are presented as pg per mg of protein. The data are presented as histograms of the means and standard errors in each group (n=3-5 per group).

Supplemental Figure 3.

A. Flow cytometry gating strategy. Gating was based on size and granularity, and CD45, TCRβ, F4/80, Ly6C/G, and CD11b staining was used to separate macrophage and monocyte populations from the spleen. Fluorescence minus one (FMO) controls are shown for each fluorochrome used.

B. Flow cytometric analysis of erythroid lineage and dot plot histogram data. The gating for erythroid progenitor populations in whole spleen, bone marrow or blood was based on the size and the expression of the differentiation marker CD71 (*i.e.*, TfR1) and the erythroid lineage marker Ter119. The relative percentages of cells in stages I-IV of erythropoiesis: stage I single-positive $CD71^{+}$ $Ter119^{-}$ early-stage proerythroblasts (region I), stage II double-positive $CD71^{High}$ $Ter119^{+}$ late-stage basophilic erythroblasts (region II), $CD71^{low}$ $Ter119^{+}$ polychromatic and orthochromatic erythroblasts (regions III and IV) and single-positive $CD71^{-}$ $Ter119^{+}$ $CD11b^{+}$ (region IV). The data are from the spleen (n=8), bone marrow (n=10) and blood (n=9) in *LysM-Atg5*$^{-/-}$ and WT mice. The data are presented as the mean and standard error values, with dots indicating individual measurements; *p < 0.05, **p=0.01, ***p=0.001, ****p=10^{-4}.

Supplemental Figure 4.

A. **Bone marrow. i**, Calcein-AM loading was analyzed by flow cytometry to measure the labile iron pool in bone marrow cells from *LysM-Atg5*$^{-/-}$ and WT mice. Immediately after recovery, cells dissociated from the bone marrow were stained simultaneously with calcein acetoxymethyl ester (CA-AM) and anti-mouse PerCP-conjugated CD11b and PE-Cy7-conjugated Ly6C/G antibodies and were then analyzed by flow cytometry. Gates were set on SSC-A and FSC. Representative calcein fluorescence profiles of unstained cells (FMO-calcein), and calcein-AM-stained cells (WT and *LysM-Atg5*$^{-/-}$) with respect to cell markers are shown, and histograms with the mean and standard error from 3 independent experiments are shown. **ii.** Detection of ferroportin by immunofluorescence in isolated cells from the bone marrow of *LysM-Atg5*$^{-/-}$ and WT mice. Representative images are composites of ferroportin (red) and DAPI-stained nuclei (blue) from 4 animals per group. Leica fluorescence microcopy imaging; original magni*fi*cation 20x; Scale bars, 20 µm. Enlarged inset images magnification, 100 x ; Scale bars 5 µm.

B. Liver. Histological examination of nonheme iron deposits after Perl's staining (blue) in liver sections in *LysM*-Atg5$^{-/-}$ and WT mice (left). Representative images from 10 animals per group are shown. NanoZoomer scan imaging, original magnification 20x ; Scale bars 100 µm.

Detection of ferroportin by immunofluorescence from *LysM-Atg5*$^{-/-}$ and WT mice (right). Representative images are composite from ferroportin (green) and DAPI stained nuclei (blue) from 4 animals per group. Zeiss fluorescence inverted microcopy imaging, original magnification 20x ; Scale bars 50 µm.

C. Tissue iron analyses. ***i***, Histological examination of nonheme iron in the kidney, heart, pancreas, and testis from *LysM*-Atg5$^{-/-}$ and wild-type mice. Representative images of Perl's staining (blue) followed by DAB enhancement (brown) are shown from 6 animals per group. NanoZoomer scan imaging, original magnification 20x; Scale bars 60 µm. **ii**, Iron content in tissue from *LysM*-Atg5$^{-/-}$ and wild-type (n = 6-10 in each group) mice, as determined by a ferrozine assay and reported as mg of dry tissue; **iii**, organ weight-to-body weight ratios.

D. Dot blotting of serum hepcidin from WT mice. Three samples of 5 µL of serum, or 10% of dry milk in solution as controls, were spotted. Samples of WT mice fed standard diet, iron deficient diet (0.5 g iron/ kg diet) or iron rich diet (25 g iron/ kg diet) for two weeks are shown. Hepcidin protein was detected using a specifc rabbit anti-hepcicin-25 antibody.[59] Densitometric analysis was performed on 6 samples per group and p values are given.

*p < 0.05, **p<0.01, ***p<0.001, ****p<10^{-4}.

Supplemental Figure 5.

A. Cell viability assayed by Hoechst 33342 DNA staining, membrane integrity assayed by lactate dehydrogenase (LDH) release assay, mitochondrial dehydrogenase activity assayed by MTT assay and cellular activity determined by glucose uptake assay. BMDMs cultured in medium without M-CSF for 24 h were then treated with FAC (100 µM), holo-TF (30 µM), oRBCs (5 red cells per macrophage). The cell count was assessed by Hoechst 3342 (20 µg/mL) nuclear staining, membrane integrity was assessed by a lactate dehydrogenase assay, an MTT assay was employed to assess mitochondrial activity, and glucose uptake activity in cells was assessed. The data are presented as the relative percentages with respect to untreated control cells (representative data from 3 experiments).

B. Flow cytometric analysis of TfR1 ($CD71^{+}$) membrane expression on BMDMs. BMDMs cultured as previously indicated were incubated with BV510 anti-CD45, PE-Cy7 F4/80 and eFluor450 CD71 anti-mouse antibodies and analyzed by flow cytometry (representative data from 3 experiments).

Supplemental Figure 6.

A. i, Perl's/DAB iron staining in BMDMs treated with oRBCs. NanoZoomer scan imaging; original magnification 20x. BMDMs from *LysM-Atg5*$^{-/-}$ and WT mice seeded on slides were incubated in medium or with opsonized red blood cells for 16 h and were fixed with PFA for immunostaining or with methanol for Perl's staining followed by DAB enhancement. **ii,** Detection of ferroportin by immunofluorescence. Images are composites of ferroportin (*red)* and DAPI-stained nuclei (blue). Leica fluorescent microscopy imaging*;* original magnification, 100x. The representative images shown are from 4 independent experiments.

B. Immunofluorescence colocalization of ferroportin in BMDMs from WT mice treated with oRBCs. WT BMDMs were double-labeled with a rabbit anti-Fpn antibody and Alexa Fluor 488-conjugated secondary donkey anti-rabbit IgG (red), followed by rabbit anti-Atg5 antibody and TRITC-conjugated goat secondary anti-rabbit IgG (green). The cell nuclei were stained with DAPI (blue). Erythrophagocytosis resulted in colocalization of ferroportin and Atg5 in most WT cells. Leica fluorescence microcopy imaging, original magni*fi*cation 40x. The representative images shown are from 2 independent experiments.

C. Immunofluorescence colocalization of ferroportin and hepcidin in BMDMs from *LysM-Atg5*$^{-/-}$ and WT mice treated with oRBCs. WT and *Atg5*$^{-/-}$ BMDMs were double-labeled with a rabbit anti-ferroportin antibody and Alexa Fluor 488-conjugated secondary donkey anti-rabbit IgG (red), followed by rabbit anti-hepcidin antibody[59] and TRITC-conjugated secondary goat anti-rabbit IgG (green). The cell nuclei were stained with DAPI (blue). Leica fluorescence microcopy imaging, original magni*fi*cation 40x. The representative images shown are from 2 independent experiments.

Supplemental Table 1. Primers of autophagy-related gene 5 (*Atg5*), Lysozyme M (*LysM*), hepcidin (*Hamp*), ferroportin (*Fpn*), ferritin –h (*Ft-H*), and erythroferrone (*Fam132b*) used for PCR and qPCR.

Atg5 forward WT allele	5'-GAATATGAAGGCACACCCCTGAAATG-3'
Atg5 forward *floxed* allele	5'-ACAACGTCGAGCACAGCTGCGCAAGG-3'
Atg5 reverse common primer	5'-GTACTGCATAATGGTTTAACTCTTGC-3'
LysM forward common primer	5'-CTTGGGCTGCCAGAATTTCTC-3'
LysM reverse WT allele	5'-TTACAGTCGGCCAGGCTGAC-3'
LysM reverse *cre* allele	5'-CCCAGAAATGCCAGATTACG-3'
Hamp1 forward	5'-CCTATCTCCATCAACAGATG-3'
Hamp1 reverse	5'-TGCAACAGATACCACACTG-3'
Fpn forward	5'-CTCTGTCAGCCTGCTGTTTG-3'
Fpn reverse	5'-TCAGGATTTGGGGCCAAGATG -3'
Ft-H forward	5'-GCCAGAACTACCACCAGGAC-3'
Ft-H reverse	5'- TGGTTCTGCAGCTTCATCAG-3
Fam132b forward	5'-ATGGGGCTGGAGAACAGC-3'
Fam132b reverse	5'-TGGCATTGTCCAAGAAGACA-3'

Supplemental Table 2. Antibodies used for flow cytometry, immunofluorescence (IF), western blot (WB) and dot blot analysis

APC anti-mouse Ter119, clone: Ter119	Biolegend, San Diego, CA
eFluor 450 anti-mouse CD71 (Transferrin Receptor), Clone: R17217 (R17 217.1.4)	Thermo Fisher Scientific, Waltham, MA, USA
PE rat anti-CD11b, clone: M1/70	BD Biosciences, Franklin Lakes, NJ, USA
PE-cy7 anti-mouse F4/80, clone: BM8	Biolegend,
PE-Cy7 Ly6C/G, clone H1/70	BD Biosciences
PercP Cy5.5 hamster anti-mouse TCRβ chain, Clone: H57-597	BD Biosciences
BV510 rat anti-mouse CD45, Clone: 30-F11	BD Biosciences
Purified rat anti-mouse CD16/CD32 (Mouse BD Fc blocker), clone: 2.4G2	BD Biosciences
PE anti-mouse F4/80, clone 6F12 (IF 1:200)	BD Biosciences
Rabbit anti-ferroportin, MTP11A (0.85 mg/mL; IF 1:500, WB 1:1000)	Alpha Diagnostics, San Antonio, TX, USA
Rabbit anti-ferritin monoclonal, clone SC0620 (1 mg/mL; IF 1:500, WB 1:2000)	Thermo Fisher Scientific
Rabbit polyclonal anti-HIF2α (1 mg/mL; WB 1:1000)	Abcam, Cambridge, UK
Rabbit anti-p62/SQSTM1 (1 mg/mL; WB 1:1000)	Sigma, St Louis, MO, USA
Rabbit anti-LC3A (1 mg/mL; WB 1:500)	Sigma
Rabbit anti-APG5/ATG5 (0.37 mg/mL; IF 1:1000, WB 1:1000)	Abcam
Rabbit polyclonal anti-hepcidin-25 (0.2 mg/mL ; IF 1 :200 ; dot blot 1:500)	Abcam (ref 59)
Secondary Alexa Fluor 488-conjugated goat anti-rabbit IgG H+L (2 mg/mL; IF 1:200)	Thermo Fisher Scientific
Secondary Alexa Fluor 488-conjugated donkey anti-rabbit IgG (2 mg/mL; IF 1:200)	Abcam
Secondary TRITC-conjugated goat anti-rabbit IgG (IF 1:200)	Sigma
Goat anti-rabbit IgG conjugated to horseradish peroxidase (WB 1:5000)	Cell signaling, Danvers, MA, USA
Mouse anti-rabbit β-actin-HRP for normalization (WB 1:5000)	Sigma
Rabbit anti-mouse GAPDH (0.167 mg/mL; WB 1:4000)	Abcam

Supplemental Table 3. Quantitative analysis of western blots from Figure 5Ai. The results were normalized to the WT control group average. The data are presented as means ± standard errors. *p* values are calculated for *Atg5*$^{-/-}$ *v.s.* WT values.

		Control	**FAC**	**TF**	**oRBC**
p62	WT	1.0 ±0.018	0.6 ±0.14	1.1 ±0.16	1.5 ±0.10
	Atg5$^{-/-}$	3.5 ±0.97	3.6 ±1.12	3.8 ±0.71	3.7 ±0.70
	p	0.011	0.01	0.003	0.006
Fpn	WT	1.0 ±0.08	0.41 ±0.04	1.7 ±0.22	1.6 ±0.22
	Atg5$^{-/-}$	2.5 ±0.06	2.36 ±0.50	2.7 ±0.19	3.8 ±0.38
	p	0.000013	0.0025	0.004	0.001
Ft-H	WT	1.0 ±0.23	5.3 ±1.22	1.4 ±0.25	6.5 ±1.52
	Atg5$^{-/-}$	1.28 ±0.08	4.6 ±0.84	1.4 ±0.06	4.1 ±0.58
	p	0.12	0.45	0.99	0.06
HO-1	WT	1.0 ±0.29	4.5 ±0.81	0.6 ±0.07	2.1 ±0.23
	Atg5$^{-/-}$	1.4 ±0.39	3.8 ±0.23	0.8 ±0.25	2.8 ±0.43
	p	0.23	0.22	0.25	0.068

Supplemental Table 4. Quantitative analysis of western blots from Figure 5C. The results were normalized to the WT control group average. The data are presented as means ± standard errors. *p* values are calculated for *Atg5*$^{-/-}$ *v.s.* WT values, but LC3AII *p* values are calculated for treated WT *v.s.* control WT values.

oRBC (Hours)		**-**	**0.5**	**1**	**2**	**4**	**8**	**16**	**24**
Hif-2α	WT	1 ±0.32	40 ±2.17	27 ±2.82	34 ±1.18	31 ±0.82	7.4 ±0.99	9.7 ±0.54	4.8 ±0.18
	Atg5$^{-/-}$	0.63 ±0.13	22 ±2.49	35 ±2.42	25 ±3.4	13.4 ±0.64	7.5 ±0.24	2.88 ±0.05	2.04 ±0.06
	p	0.4	0.07	0.16	0.19	0.055	0.44	0.023	0.054
p62	WT	1 ±0.05	0.3 ±0.02	0.42 ±0.01	0.41 ±0.02	0.67 ±0.05	1.43 ±0.07	0.75 ±0.03	0.74 ±0.05
	Atg5$^{-/-}$	2.1 ±0.32	0.4 ±0.017	0.7 ±0.17	0.46 ±0.01	1 ±0.21	1.7 ±0.33	2 ±0.3	2.2 ±0.02
	p	0.0002	0.092	0.0036	0.87	0.012	0.03	0.0015	0.00005
LC3AI	WT	1 ±0.32	0.19 ±0.04	0.32 ±0.03	0.47 ±0.08	0.51 ±0.09	0.45 ±0.03	0.53 ±0.08	0.44 ±0.07
	Atg5$^{-/-}$	0.61 ±0.09	0.19 ±0.03	0.14 ±0.02	0.18 ±0.02	0.16 ±0.03	0.45 ±0.04	0.72 ±0.1	0.81 ±0.15
	p	0.33	0.68	0.21	0.11	0.12	0.86	0.47	0.21
LC3AII	WT	1 ±0.49	1.25 ±0.07	4.6 ±0.48	6.3 ±0.39	8.2 ±0.59	22.8 ±0.99	35.4 ±5.2	24 ±3.15
	p	-	0.99	0.99	0.98	0.91	0.73	0.0015	0.038
Fpn	WT	1 ±0.01	345 ±18	511 ±53	305 ±10	230 ±5.8	72 ±9.7	9.1 ±0.5	18 ±0.7
	Atg5$^{-/-}$	425 ±32	602 ±172	322 ±42	410 ±125	365 ±54	130 ±21	81 ±17	372 ±89
	p	0.000014	0.0183	0.1565	0.4135	0.0086	0.0015	0.000008	0.000032

Supplemental figure 1

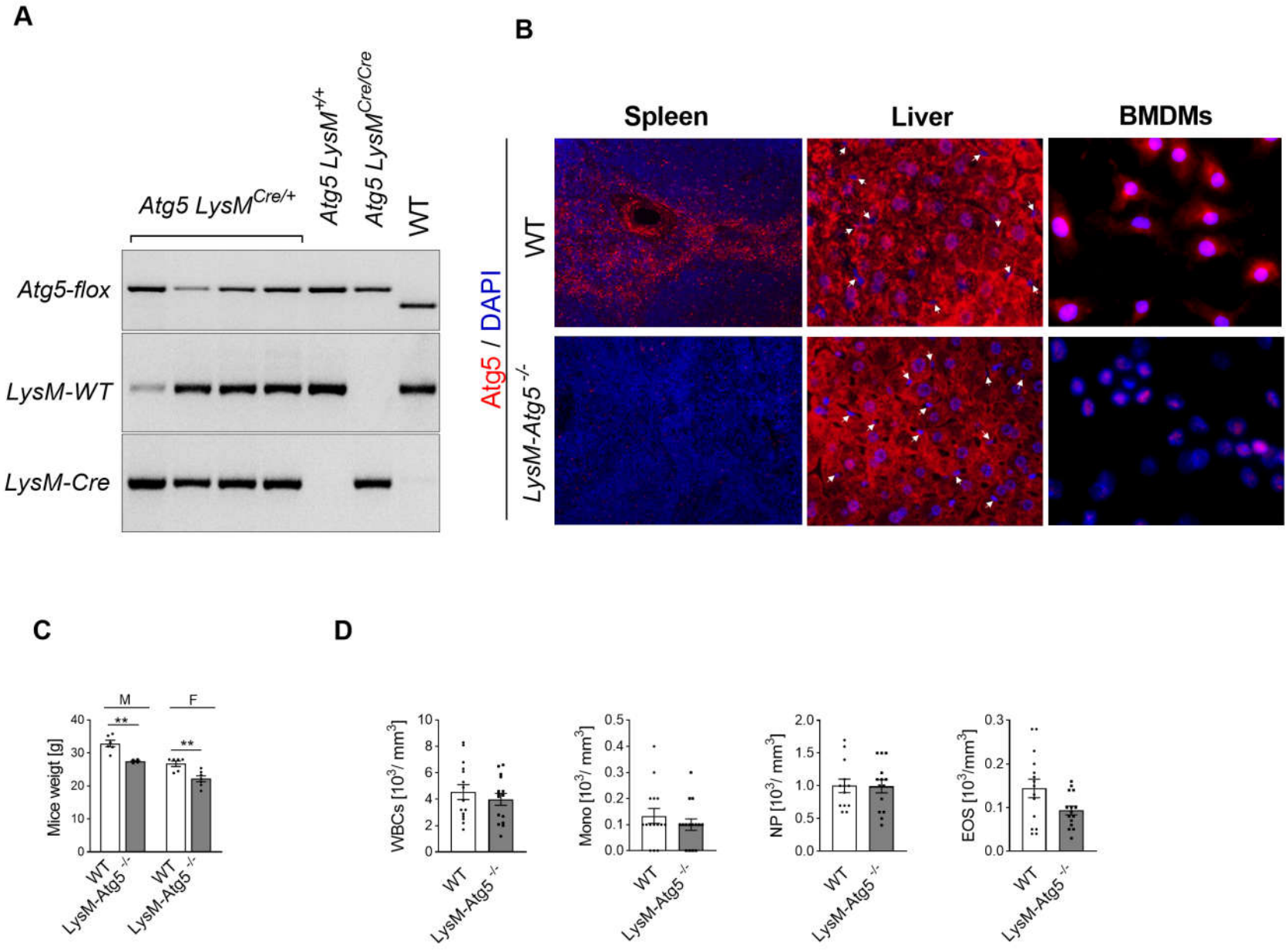

Supplemental figure 2

A Liver

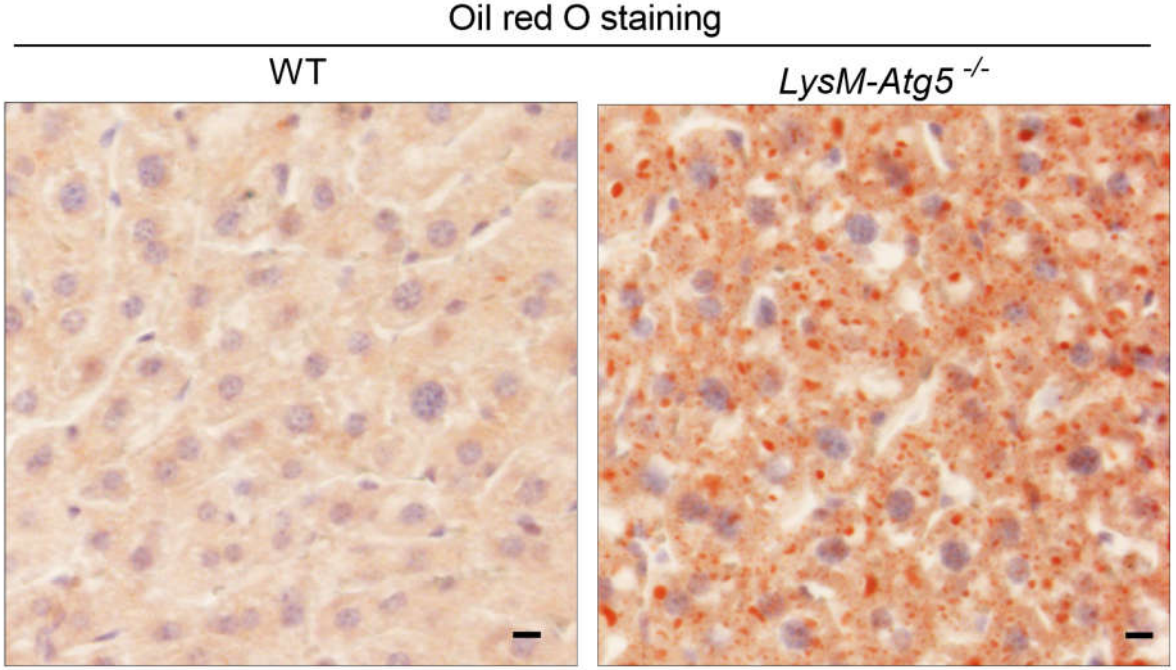

B

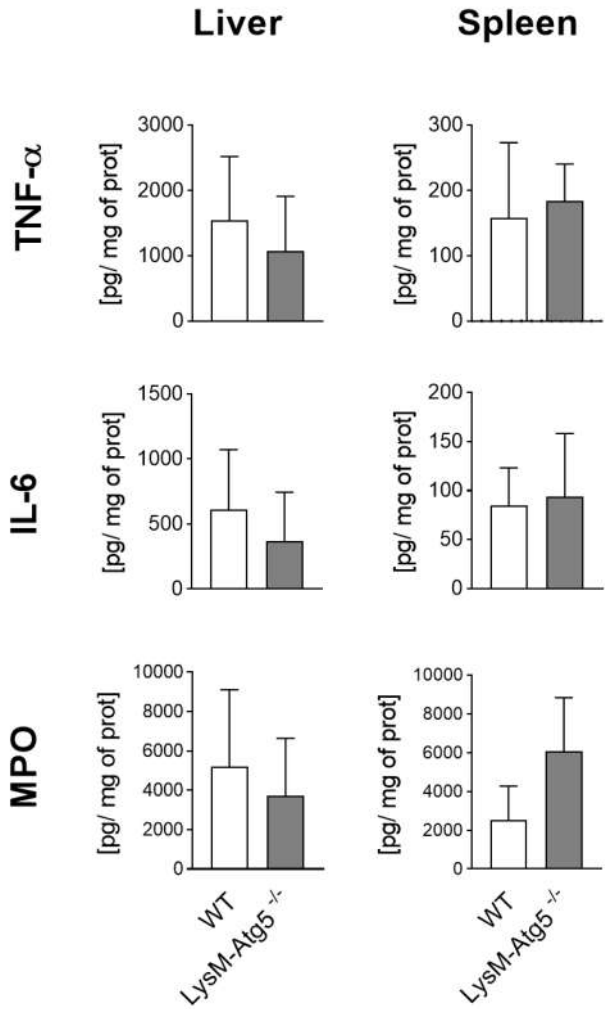

Supplemental figure 3

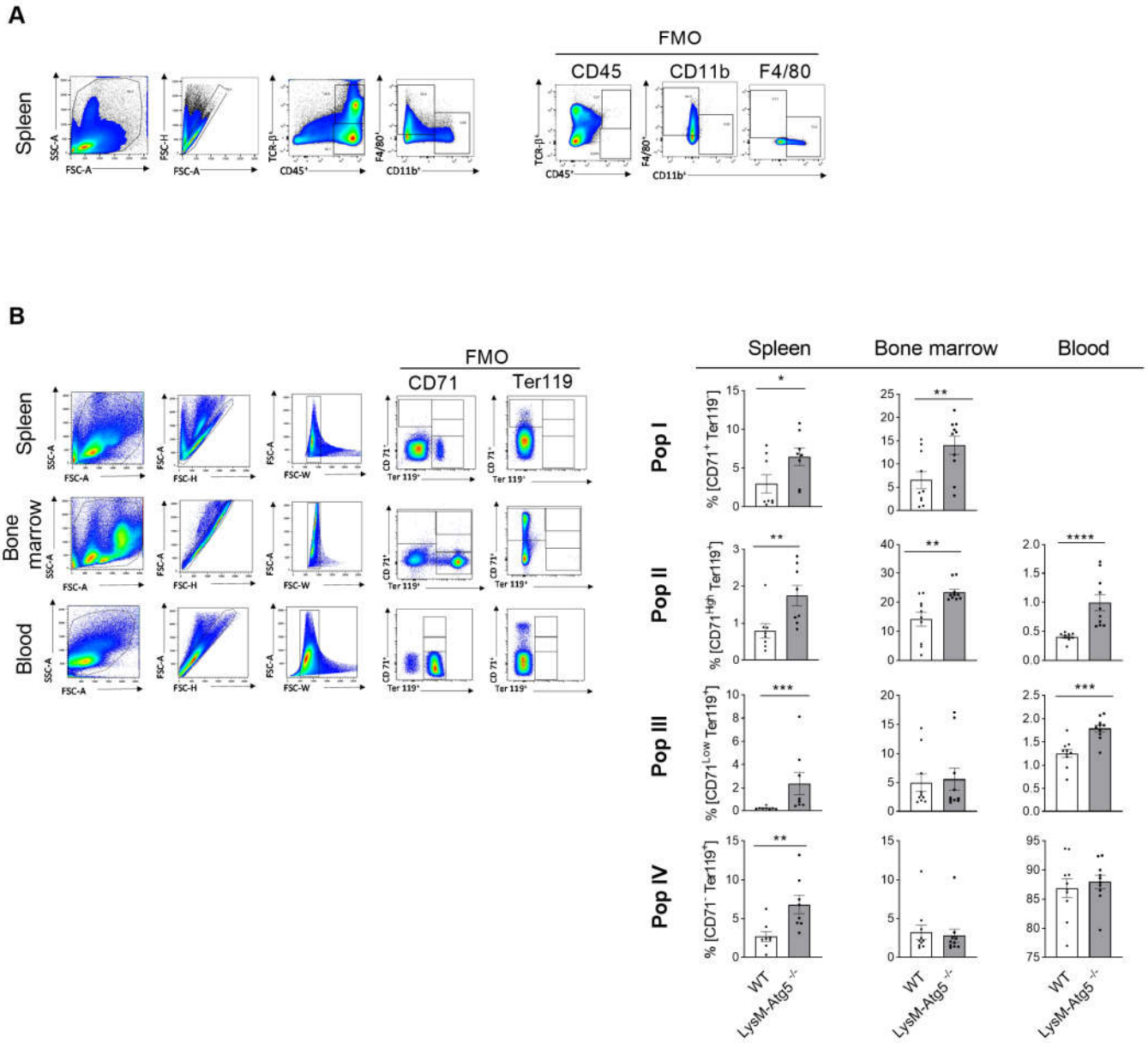

Supplemental figure 4

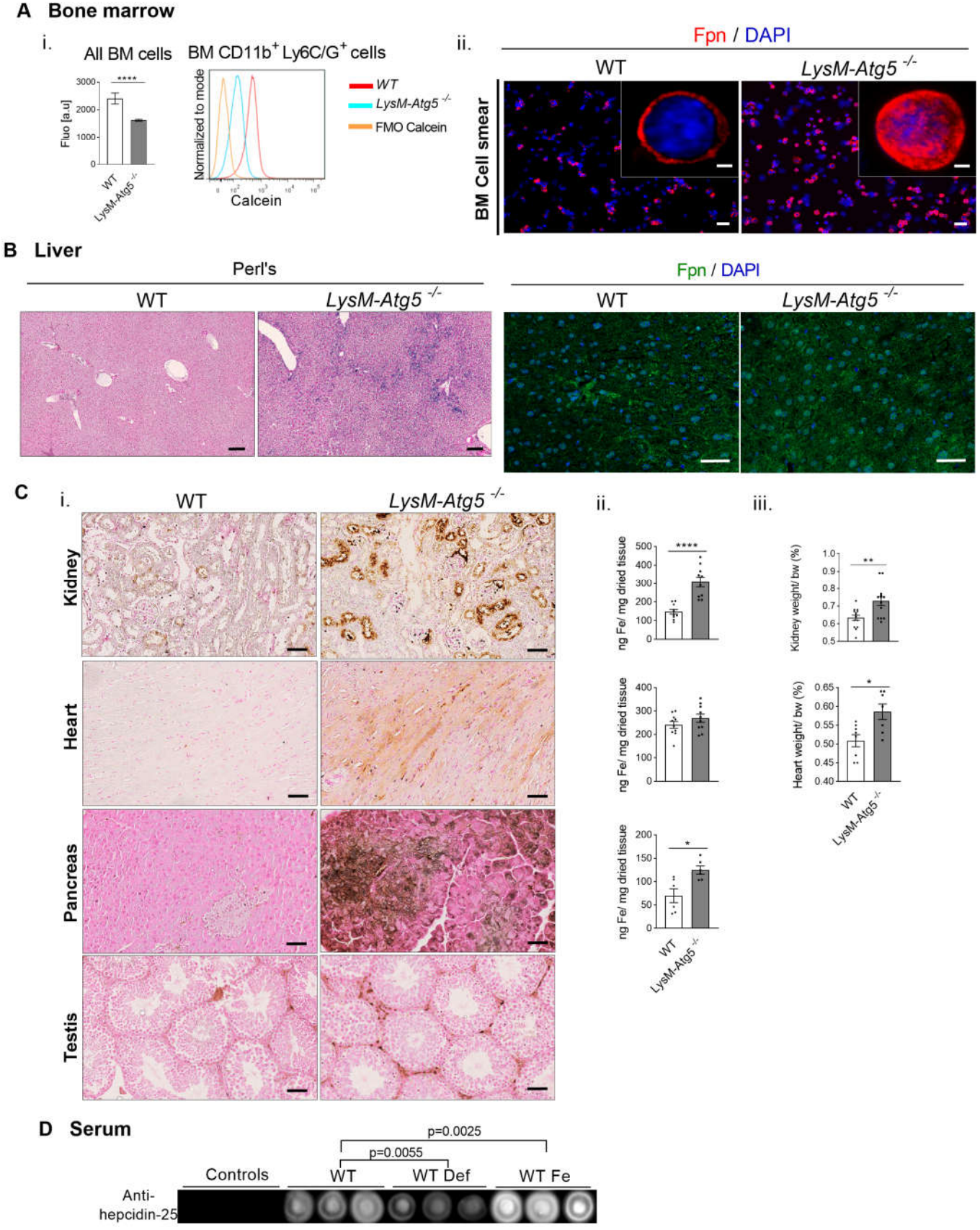

Supplemental figure 5

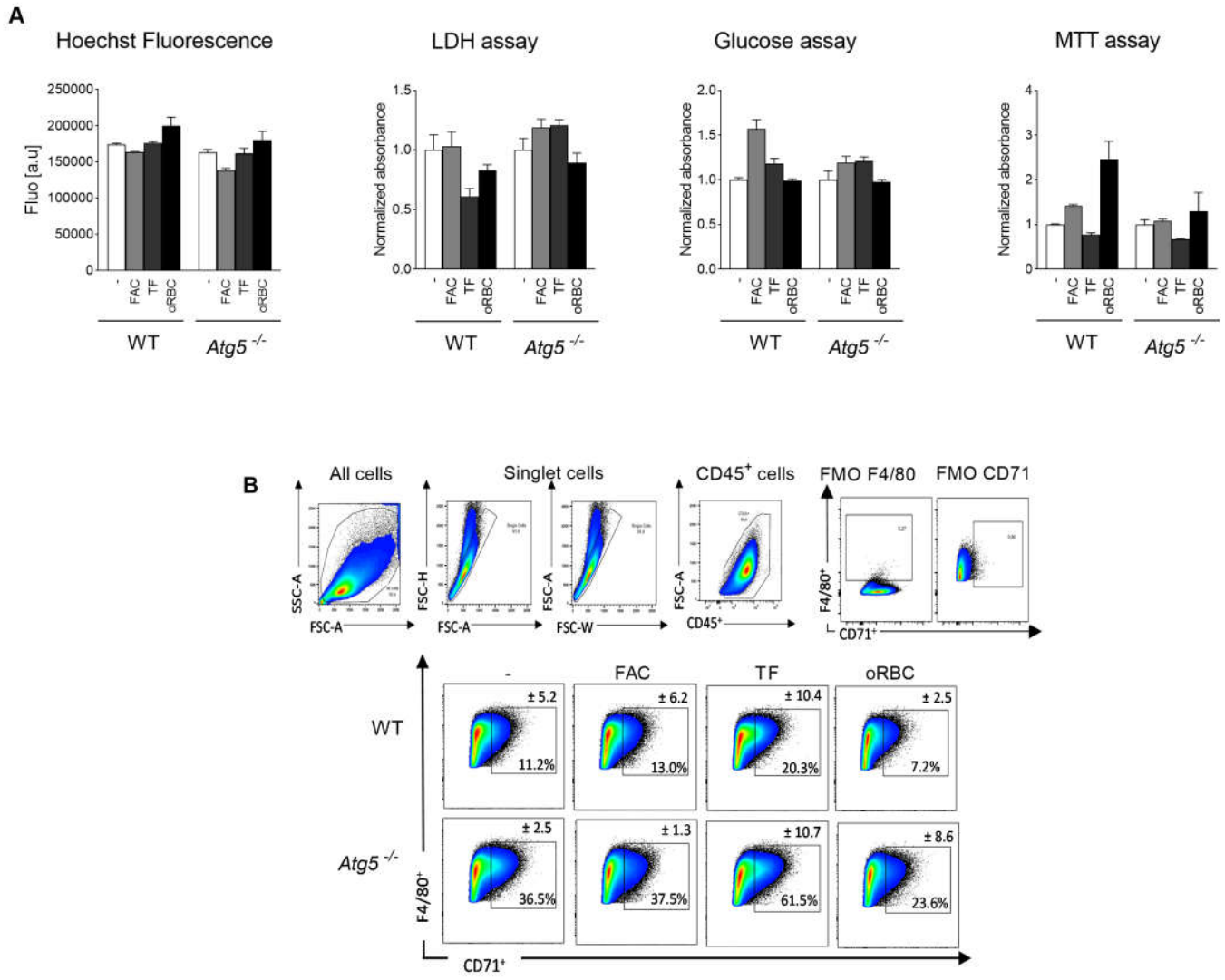

Supplemental figure 6

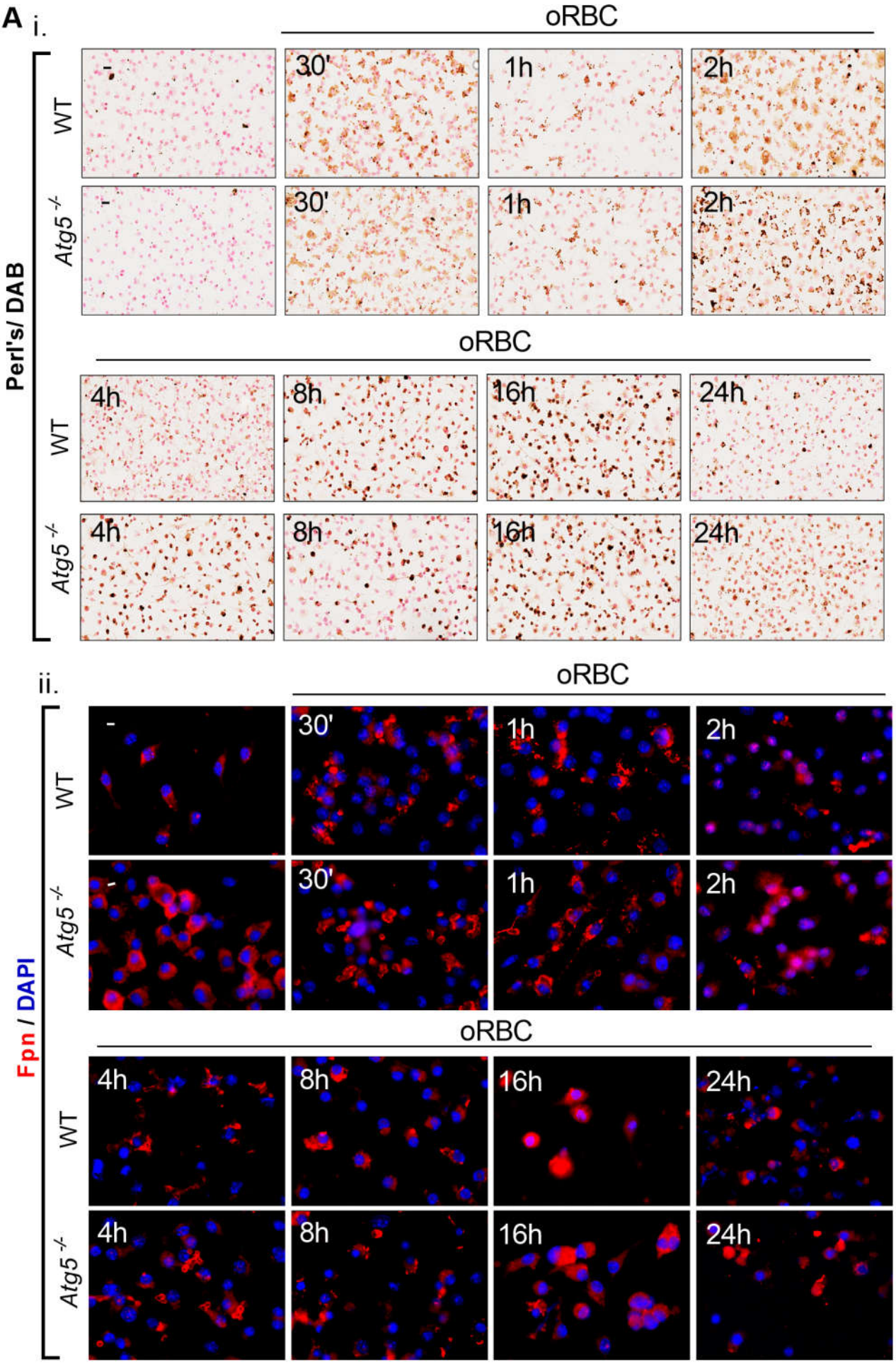

Supplemental figure 6